2005

Performance evaluation of two CZT gamma ray imaging systems

Laurie Kelly
Louisiana State University and Agricultural and Mechanical College, lkelly3@lsu.edu

PERFORMANCE EVALUATION OF TWO CZT GAMMA RAY IMAGING SYSTEMS

A Thesis

Submitted to the Graduate Faculty of the
Louisiana State University and
Agricultural and Mechanical College
in partial fulfillment of the
requirements for the degree of
Master of Science

in

The Department of Physics

by
Laurie Anne Kelly
B.S., University of New Orleans,2002
August 2005

This work is dedicated to my daughter,
Sophia Surreal Davis.

Acknowledgements

I would like to thank Dr. Kip Matthews for providing such an excellent learning environment both during my thesis work as well as over my entire experience at LSU. I will always be grateful for his tireless enthusiasm for research and teaching, his patience at explaining often times difficult subjects and his willingness to help all students.
I could not have had a more supportive or knowledgeable advisor.

I would also like to thank the other members of my thesis committee for their input and time, Dr. Wei-Hsung Wang, Dr. Greg Guzik, Dr. John Gibbons, Dr. Erno Sajo, and Dr. Kenneth Hogstrom

Thanks to Yvonne Thomas who provided much assistance keeping everything running smoothly. Thanks to Blair Smith and John Richert for their help in proof reading and offering corrections. Thanks to Ken Bernstein for being a compadre during the hardest parts of the journey.

I would like to thank my parents, Judy and Dennis Kelly, who believed in me and have supported me through thick and thin. Thanks to my daughter, Sophia Surreal Davis for laughter and love and keeping me human.

Table of Contents

List of Tables

List of Figures

Abstract

The purpose of this research was to evaluate the performance of the imaging characteristics of two versions of a cadmium zinc telluride (CZT) gamma radiation detector system called the Laboratory Radioactive Assay Tracer (LabRAT). The performance evaluation follows the National Electrical Manufacturers Association standards for pixellated detector cameras. The LabRAT detector system hardware was developed by Mosaic Imaging Technology, Inc. LabRAT is a portable nuclear medicine imaging detector system intended for small field of view applications such as small animal imaging, portable radioisotope imaging in emergency room or intensive care units, and as an instruction tool for radiology residents and physics students. The tests performed include the measurement of count rate performance, per-pixel and composite energy resolution, uniformity of detector response, extrinsic spatial resolution, linearity, and integral and differential uniformity. Prior to the performance evaluation acquisition software was developed to operate the detector, including initializing the detector, performing data acquisition and displaying images and energy spectra. One of the systems had a better composite energy resolution due to the fact that the locations of photopeak centers for the individual pixels in that detector were consistently more uniform than the locations for the other detector. The energy resolution attainable for individual pixels is good, but due to limitations in user control over tuning of individual pixels, the composite energy resolution values were higher than expected for both systems. In practice, energy

windows must be applied on a per-pixel basis. Spatial uniformity is worse than for typical scintillator-based gamma cameras, while extrinsic spatial resolution is satisfactory.

Chapter 1

Introduction

The focus of this research is the performance evaluation of two bench top cadmium zinc telluride (CZT) gamma-ray imaging systems nicknamed LabRAT or the Laboratory Radioactive Assay Tracer system. The specific details of these systems are given in Chapter 2. Figure 1 and Figure 2 show the two systems; the system in Figure 2 is an updated version of the original system shown in Figure 1.

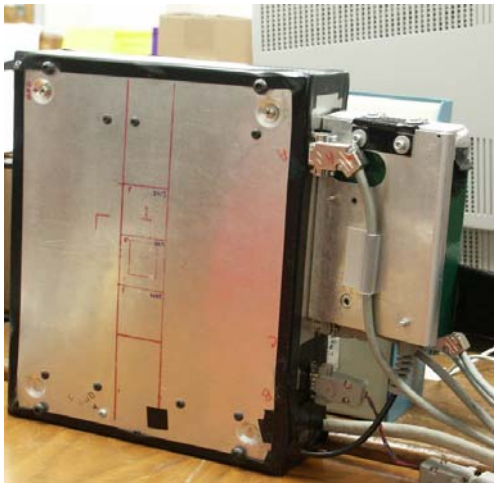

Figure 1. Photograph of LabRAT version 0 detector.

Figure 2. Photograph of LabRAT version 1 detector.

1.1 Background on Gamma Cameras

Gamma cameras are used in nuclear medicine to provide functional imaging of patients. The patient is given a radiopharmaceutical which emits gamma radiation. The patient is positioned so that as the radiation exits their body it is detected by the gamma camera. Typically the detecting material used in gamma cameras has been crystals composed of sodium iodide doped with thallium (NaI(Tl)). These type of cameras require an array of photomultiplier tubes to accurately reconstruct the position where incoming radiation events occurred, thereby constructing a useful image of the patient [5]. The NaI(Tl) crystals are large in order to enable whole body imaging and the crystal and photomultiplier tube assembly must be shielded with lead. This results in a very heavy detector assembly. These type of gamma or Anger cameras as they are also called have been in use for many decades [5].

One problem with NaI(Tl) is that its energy resolution is not ideal; typical values are 9-10% at 140 keV [1,2]. Due to their superior energy resolution (~4-8% at 140 keV) CZT detectors, such as LabRAT are being studied as a possible alternative to NaI(Tl) detectors in the field of nuclear medicine due to the superior energy resolution possible with CZT. Another difference between NaI(Tl) detectors and CZT detectors is that the CZT detector modules are small, solid state semiconductor crystals which do not require photomultiplier tubes and require less lead shielding. A much lighter and more compact detector for a given field of view is possible with CZT as opposed to the NaI(Tl) based gamma camera.

1.2 Motivation and Goals

The motivation for this work is to measure the imaging characteristics of the LabRAT systems. The detector hardware was designed and built by Mosaic Imaging Technology, Inc., with collaboration by my advisor, Dr. Matthews. Some rudimentary software had also been written. A performance evaluation had never been done for these systems. LabRAT 1 uses an updated version of some of the detector electronics whereas LabRAT 0 uses an older version of these same components. It is expected that the energy resolution, uniformity of detector response and possibly the count rate performance should be better for LabRAT 1 than for LabRAT 0, because of improvements made in the detector electronics. Linearity and spatial resolution should be similar due to the fact that these measurements are intrinsic to the detector crystals and should not be greatly affected by a change in detector electronics. To do the performance evaluation it was necessary to first develop computer software to run the detector acquisition routines. Then we performed the data acquisition and analysis necessary to characterize the systems. Thus, the specific aims of this thesis are

1. To develop acquisition software
    A. Update the initialization code.
    B. Develop the acquisition code.
    C. Improve the user interface.

and

2. To acquire and analyze performance evaluation data
    A. Tune the detector system.

B. Identify NEMA performance standards relevant to monolithic crystal, position sensitive CZT systems such as LabRAT.

C. Acquire and evaluate performance data.

The programming required writing image acquisition software to produce real-time images and implementing the ability to use up to 25 CZT detector modules in one system (a detector module consists of a monolithic CZT crystal, the pins to attach it to a carrier board and the electronics necessary to process radiation interaction events). It was also necessary to develop a graphical user interface and update existing initialization code to accommodate a new version of the detector modules (the difference between the two types of modules is discussed in section 2.2.2). Pre-existing software for the systems provided only rudimentary data acquisition and could not operate the new detector modules; event processing and image display occured off-line.

The performance evaluation was carried out in accordance with the National Electrical Manufacturers Association (NEMA) guidelines for gamma cameras. These guidelines are set forth in NEMA NU-1 [3]. This handbook gives a "uniform criterion for the measurement and reporting of [gamma camera] performance parameters by which a manufacturer may specify their device."

The specific tests that were performed on the LabRAT systems are listed below; each will be discussed in detail in Chapter 5.

1. Count rate performance.
2. Energy resolution for each pixel as well as for the detector system as a whole.
3. Spatial resolution as a function of position.

4. Linearity.
5. Flood field uniformity.

1.3 Outline of Thesis

Chapter 2 gives background information on CZT as a detector material and describes the structural and functional details of the LabRAT systems. In Chapter 3 an overview is given of the programming for the LabRAT systems. Chapter 4 discusses the need to tune the detector and the method for doing so. The details about the methods, materials and results for the performance evaluation are given in Chapter 5. The discussion, conclusion and future work are discussed in Chapter 6.

Chapter 2

Background

2.1 CZT as a Radiation Detector

Semiconductors, such as CZT, have desirable properties with regard to radiation detection; these include better energy resolution than NaI(Tl) and good detection efficiency due to a high effective atomic number (Ca is 48, Zn is 30 and Te is 52). CZT unlike some other semiconductors has the added benefit of room temperature operation which allows for small, lightweight detector designs. CZT was developed as an improvement on CdTe which has been in use as a semiconductor detector since its development by De Nobel *et al.* in 1958 [4]. Although CdTe detectors have good detection efficiency and can be operated at room temperature, CdTe has relatively high leakage currents that lead to blurring of the low energy side of spectra. CdTe is also expensive to produce. By adding small amounts of zinc as a dopant, both of these problems are reduced, although there continue to be problems concerning purity and homogeneity for production of CZT [4].

Position sensistive CZT detectors for nuclear medicine imaging can either be truly pixelated or can be composed of monolithic crystal or pieces of crystals with pixelation defined by the anode contacts on the crystal (this is the case with the detectors used in the LabRAT systems). Figure 3 is an illustration of these two types of detector configurations. There are also other ways, not illustrated here, to attach the contacts on the crystals such as the orthogonal strip method [13]. In a truly pixellated detector, any

radiation interaction events that occur within a given pixel will be counted toward that pixel only. In contrast, in a monolithic crystal with pixellation due to multiple contacts on the crystal, radiation interaction events near a contact will most likely be counted towards the pixel that is defined for that contact, but events near the borders between pixels that are not directly under a given contact can result in charge being shared by more than one pixel.

The good energy resolution in CZT is a result of a large numbers of charge carrriers being produced per electron-volt of energy deposited in the material and of a low Fano factor [5]. The Fano factor is the ratio of the variance of the number of electrons actually produced to the Poisson statistical expected variance. The energy resolutions reported for many types of CZT detectors typically range from1-5% [6]. Single pixel energy resolution values as low such as 1% at 662 keV have been reported [7], but single pixel data is not indicative of detector-wide performance.

Some reported detector-wide energy resolution values are <2% for 662 keV and 3% for 122 keV by Perkins *et al.* [8]; Butler *et al.* reported <4% for 140 keV [9]. IdeAS Inc. (Norway) has developed a similar system to LabRAT; they report that their system exhibits 93% of pixels with photopeak resolution <8% for 140 keV [10].

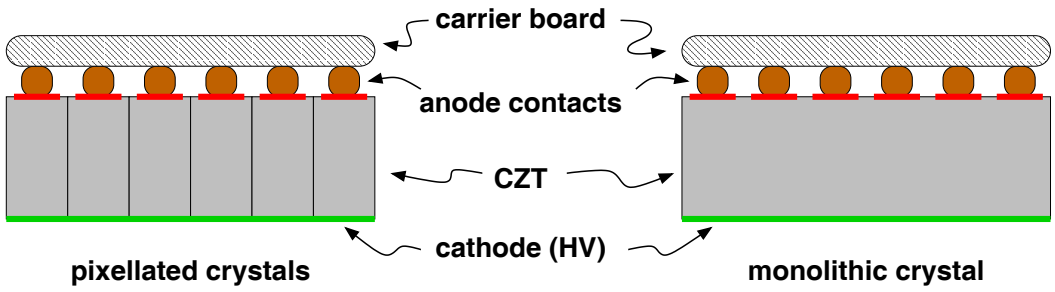

Figure 3. Illustration of side view of pixellated (left) and monolithic crystal (right) configurations for CZT detectors.

Some problems with CZT that lead to increased energy resolution values are charge carrier trapping, depth of interaction effects and boundary effects due to pixelation [4]. These contribute to the phenomenon of tailing on the low energy side of the photopeak that occurs in semiconductor detectors. Figure 4 shows an energy spectrum from LabRAT for a Tc-99m point source that demonstrates the tailing phenomenon. Imperfections in the crystal lattice of the semiconductor material cause charge carriers to become trapped before they are collected at the anode. Sato *et al.* [11] found that full collection of charge carriers in CZT is limited by the combination of short lifetimes and low mobilities especially for holes. Incomplete charge collection shifts events into the photopeak tail.

According to Schlesinger, incoming events that fall in the center of a pixel will contribute to the photopeak, while those near the boundaries will contribute to the low-energy tail [4]. Kalinosky *et al.* demonstrated that these boundary effects are due to x-ray flourescence scattering, Compton scattering and overlap of the charge cloud between pixels [12]. The charge cloud is the group of electrons and holes that results from ionizations due to x-ray interactions in the material. For energies up to 511 keV, charge clouds do not typically diffuse to larger than 250 microns in diameter [6]. A small spatial resolution using approximately 0.5 mm sampling elements could be achieved with a charge cloud of this size, but boundary effects will be more pronounced with smaller pixels because of the larger proportional area of the boundary regions. Monolithic CZT spatial resolution of 50 microns at 22 keV, 100 microns at 88 keV [13] and 100-300 microns at 60 keV [14] have been reported for astronomy applications using CZT modules that are configured as orthogonal strip detectors optimized for spatial resolution.

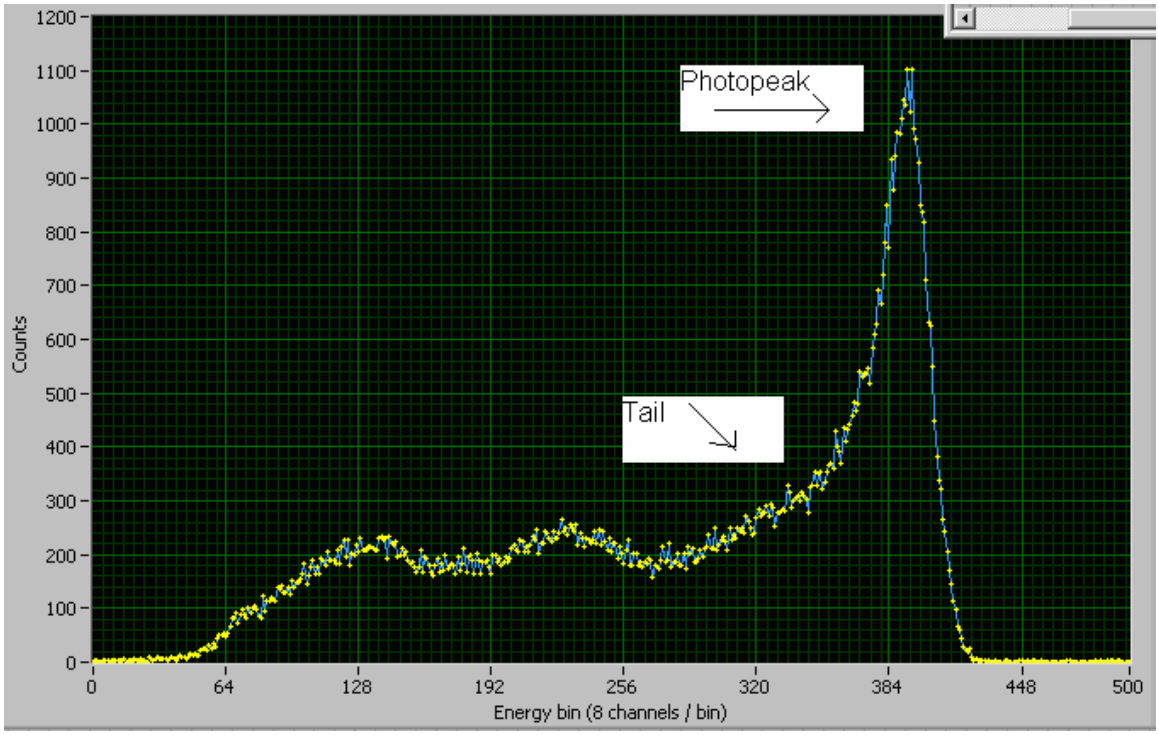

Figure 4. Energy spectrum for a Tc99m (140 keV photopeak) point source showing a shift of counts to the low energy side of the photopeak.

Currently, it is difficult to grow CZT crystals with perfect uniformity [6]. Imperfections may lead to charge trapping and problems with charge collection. Although Imarad (the manufacturer of the CZT modules used in the LabRAT systems) claims that "the volume of...a nuclear spectrometer can be made as large as one wishes, by assembling a multitude of modules" [15], at the current time the high cost of CZT detector modules (approximately $3000 per square inch for CZT crystals) restricts the field of view achievable at reasonable cost and therefore it is not currently suitable for use in large field of view imaging systems.

CZT radiation detectors are being used for security purposes with regard to radioactive materials [16,17,18] and in gamma-ray astronomy [11,14,19] as well as in

medical imaging. Work is being done on scintimammography detectors [20] using CZT and bone densitometers [21] are in use currently using CZT detectors, because both of these applications only require small fields of view. Other medical uses include miniature portable and intra-operative probes as well as detectors for cardiac imaging [22].

LabRAT is intended for use as an affordable, research-grade gamma radiation ray imaging system for small field of view applications. Uses include small animal imaging, portable radioisotope imaging in emergency room or intensive care units, and as an instruction tool for radiology residents and physics students.

2.2 Overview of LabRAT

2.2.1 Detector Layout

The LabRAT detector system hardware was built by Mosaic Imaging Technology, Inc. For LabRAT 1, detector modules and high voltage power supply are in one box and the electronics power supplies and the signal processing boards are in a separate box, as shown in Figure 5. The two boxes are connected by a ribbon cable for the data signals and a power cable to provide power from the electronics box to the detector box. The two boxes are made out of aluminum. The front plate is approximately 0.5mm thick where radiation events enter the detector.

A copper foil is mounted inside the front plate and electrically isolated from the box. The purpose of the foil is to distribute the high voltage over the cathode side of the detector modules. An aluminum framework within the box is used to hold heat sinks in contact with the detector modules to provide passive cooling. The outer dimensions of

the detector box for LabRAT 1 are 31 cm x 31 cm x 27 cm. This is much larger than is actually necessary, to allow easy access to the detectors during development work.

In LabRAT 0, the power supplies are all external, while the detector modules and signal processing boards are located together in a single 31cm x 31 cm x 8 cm aluminum box. The box provides heat sinks for cooling and a copper foil for high voltage distribution.

Figure 5. Inside view of the electronics box of LabRAT 1 showing power supplies and signal processing boards.

2.2.2 CZT Module Layout

Both versions of LabRAT contain CZT modules and components from Imarad, Ltd. [15]. Each CZT module is a 38.4 mm x 38.4 mm x 5 mm monolithic crystal divided into 16 x 16 pixels. Each pixel within the module is 2.4 mm x 2.4 mm x 5 mm. Figure 6 shows a CZT module like those used in the LabRAT systems. The pixel dimensions are determined by the size and layout of the contacts on the anode side of the crystal.

Figure 6. Photograph of an Imarad CZT module.

The pixels on each detector module are bonded to a pair of ASICs (application specific integrated circuits) that provide pulse shaping and pixel identification. Each module has two ASICs and each ASIC processes the signals for 128 pixels. Figure 7 illustrates the layout of the pixels and ASICs within each module [10]; this pixel map translates between the (x,y) location of the pixel and a unique pixel identifier determined by the connection of each pixel to its ASIC within a module.

y \ x	0	1	2	3	4	5	6	7	8	9	10	11	12	13	14	15
0	3D	9E	A2	84	86	90	81	85	9D	9B	ED	FB	FD	F9	E3	F4
1	49	37	9A	82	8A	94	83	87	91	9F	F1	F5	EB	DD	F6	E6
2	4B	41	33	80	96	9C	A5	8B	95	99	EF	F7	DB	F0	FE	E8
3	38	43	35	2F	92	98	A0	A1	8F	97	F3	FF	F2	FC	EE	DE
4	53	51	47	3B	2A	8E	8C	A8	8D	89	E5	E9	FA	F8	DF	E2
5	4A	42	4F	45	39	2D	88	A4	A7	93	E7	E1	EC	EA	E4	DA
6	4E	4C	46	4D	3E	3F	31	A6	A3	AC	AE	B0	D8	E0	DC	D9
7	44	48	52	50	55	3A	32	29	AB	B4	C8	D4	C4	D6	D0	D7
8	54	56	3C	36	34	40	30	2B	A9	B2	C0	C6	CC	CE	D2	C2
9	58	5A	62	5E	67	5D	2E	2C	18	AA	AF	BA	CB	D5	CA	BE
10	5C	60	6C	76	79	61	5B	57	0C	28	AD	BB	BF	CD	C5	C1
11	64	6A	7C	7E	71	65	5F	59	00	27	24	B3	B9	CF	C9	D1
12	66	70	72	6D	6F	69	63	01	02	0E	12	20	B1	BD	C7	D3
13	68	78	7F	6B	75	1F	21	03	0B	15	10	16	22	B7	BC	C3
14	74	7A	73	7B	23	1D	17	05	0F	13	06	0A	1C	26	B8	B6
15	6E	77	7D	25	1B	19	11	09	0D	07	04	08	14	1A	1E	B5

Figure 7. Layout and connection of pixels in an Imarad CZT detector module. Each smaller box represents an individual pixel; the bold line marks the dividing line between ASICs.

The CZT and the ASICs are mounted on a circuit board that routes power, control signals and data signals in and out of the detector module. The circuit board pin-out mates to an industry standard microprocessor socket. When purchased from Imarad, each preassembled module comprised the CZT, the ASICs and the circuit board. The ASICs in the LabRAT systems were manufactured for Imarad by Ideas ASA [10].

Two different versions of the ASIC design have been used in the LabRAT modules. The earlier detector system contains version 3.0 of the ASIC design and the more recent model contains version 3.2 ASICs. One difference between the 3.0 and 3.2 versions is that the 3.2 ASIC provides a greater range of adjustable parameters on the ASIC circuits. Another difference is that the 3.2 ASICs implement differential outputs for the energy signals while 3.0 ASICs use single-ended outputs. Each ASIC provides a preamplifier for each pixel as well as a dummy channel for the differential output. Preamplifier parameters such as the shaping time constant are set globally by the ASIC. The ASIC also provides the ability to set both an ASIC-wide voltage threshold and a per pixel voltage threshold. The ASIC circuitry allows for individual pixels to be disabled. Finally, the ASIC provides calibration inputs to each preamplifier to test their operation. During normal operation the outputs from an ASIC for a detected gamma ray are the differential signal that represents the gamma ray energy and the address of the pixel in which the gamma ray interacted. The output also includes a self-generated trigger signal and an indicator if multiple events have occurred simultaneously.

2.2.3 System Electronics: Internal Boards and DAQ Boards

The detector modules mount in sockets on a carrier board in the detector box. The carrier board, shown in Figure 8, can hold up to 25 modules in a 5 x 5 array. For our

testing, LabRAT 0 originally had 3 modules in a column, but one module is no longer functioning. The LabRAT 1 was supposed to have four modules in a 2 x 2 array; one of these modules is not functioning, so the remainder were reconfigured into three modules in a column. The carrier board routes power, control signals and data signals from the modules to the other electronics boards in the system. An illustration of the carrier board layout is given in Figure 9.

Located in the electronics box along with the power supplies are three additional electronics boards. Shown in Figure 10, one is the data processing board, another is the communications board and the third is a passive signal adapter board. The data processing board converts current-based detector outputs to voltages. A twelve-bit A/D converter digitizes the voltage signals. The signals and the pixel address information are stored in a memory buffer to await transfer by the communications board. The communications board controls serial communications between the detector system and the host computer. Control communications are sent over a standard 9-pin serial connection while the data signals are sent to the acquisition computer over a dedicated data cable. Each bit of the digitized signals is placed on one pin of the data cable. For each detected gamma event the digitized energy and pixel address are sent sequentially to the data acquisition computer.

The data cable connects to a National Instruments PCI-6534 digital I/O card and a PCI-6602 timer in the data acquisition computer [23]. The 6602 timer generates an external clock signal when the communications board indicates that pixel and energy information are available for transfer. The 6534 board reads the bit values of the pixel address and digitized energy signal. The recorded values are then transferred into

computer memory for processing into images by the acquisition software. The software is discussed in Chapter 3. The two acquisition computers being used with the LabRAT systems are Pentium-4 computers running Windows 2000.

Figure 8. Photograph of the carrier board used in the LabRAT systems. The carrier board holds up to twenty-five CZT modules.

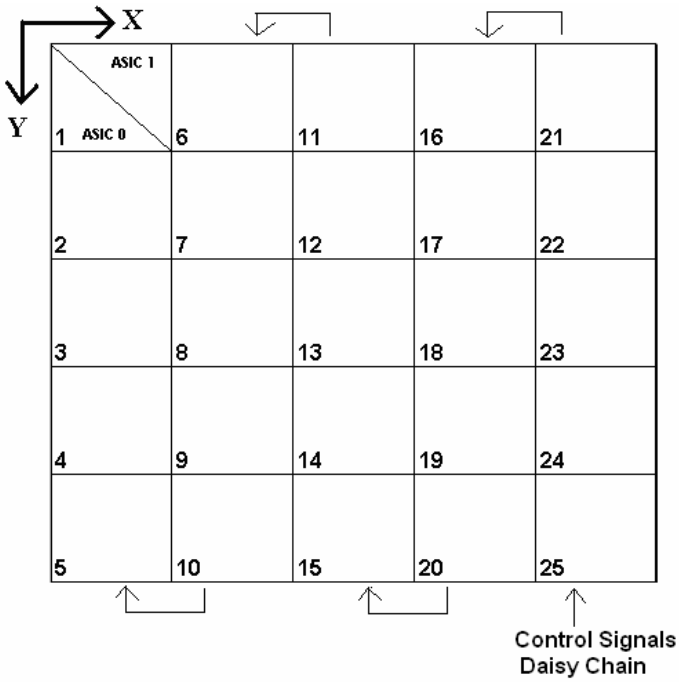

Figure 9. Illustration of the carrier board layout. The orientation of ASICs is shown for module 1 and is the same for all modules. Control signals are daisy chained serially from one module to the next as demonstrated by the sequence of arrows.

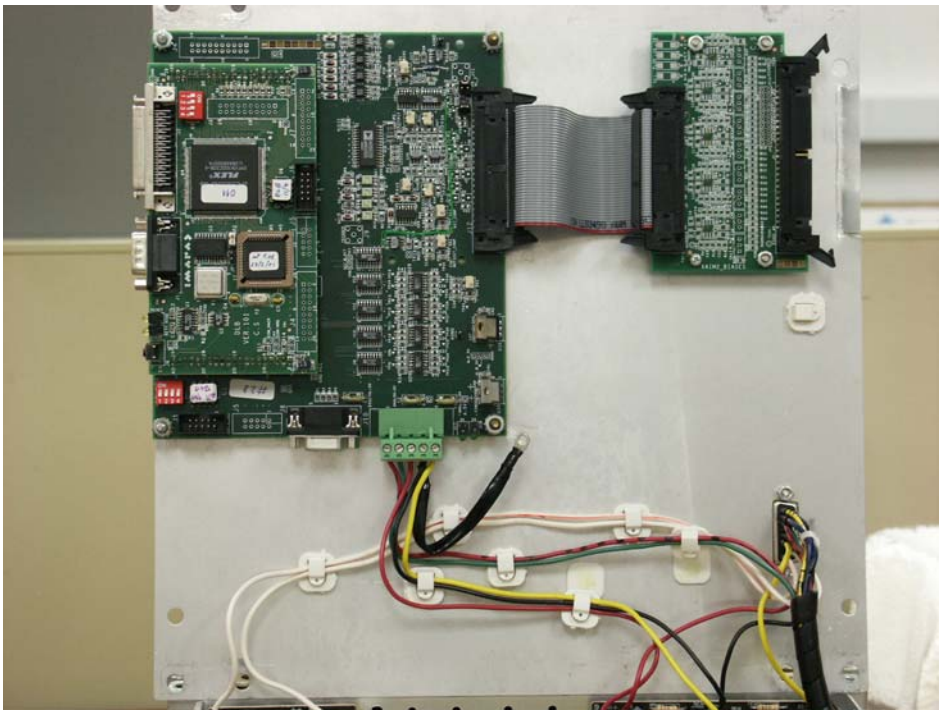

Figure 10. Three communications boards reside in the electronics box with the power supplies: the data processing board (left), the communications board (piggyback on left), and a passive signal adapter board (right).

2.2.4 Collimator and Shielding

The current LabRAT systems do not have dedicated collimators and shielding. For the purposes of minimizing design costs at the prototype stage, design of the collimator assembly has been deferred to future work. For this thesis, performance measurements requiring a collimator and shielding have been made using a piece of general-purpose, low-energy collimator and sheets of lead. These measurements are discussed in Chapter 5.

Chapter 3

LabRAT Acquisition Software

Prior to the performance evaluation, a major project task was to develop acquisition software for the LabRAT systems. The LabRAT software has three main parts and a section is devoted to the description of each.

1. Initialization: establish communication between detector and computer, load operating parameters to detector.
2. Acquisition: process incoming gamma ray interactions.
3. Image and energy spectra display: convert raw interaction data into images, save data.

The LabRAT system software is written in LabView 7.0 [23]. LabView programs and subroutines are called "virtual instruments" or VIs. The important features of each software component are described below. Additional programming related specifically to data analysis is discussed in Chapter 5. A rudimentary software package was provided by Mosaic Imaging; this software provided basic setup and accumulation of event data. While this software was useful for demonstrating detector operation, it lacked features for real-time image and spectra display, for detector tuning and for handling the new 3.2 version ASICs. The basic software was revised and expanded to create the new LabRAT system interface.

The user interface of the LabRAT software is shown in Figure 11. The user interface integrates the three main software components. User input includes controls to initialize the detector, to set initialization parameters and to set acquisition parameters such as acquisition length, stop conditions and output file name. This is the primary program used for routine image acquisition. Some minor variations on this program were used to facilitate the performance evaluation work, particularly for automating some acquisition tasks and to integrate the use of a computer-controlled translation stage. The front panels and block diagrams for these variant programs are located in Appendix A.

Output components of the LabRAT system software include display of image and energy spectrum data, which are updated as the program acquires data from gamma ray interactions in the detector. Other outputs include elapsed acquisition time, accumulated counts and count rate.

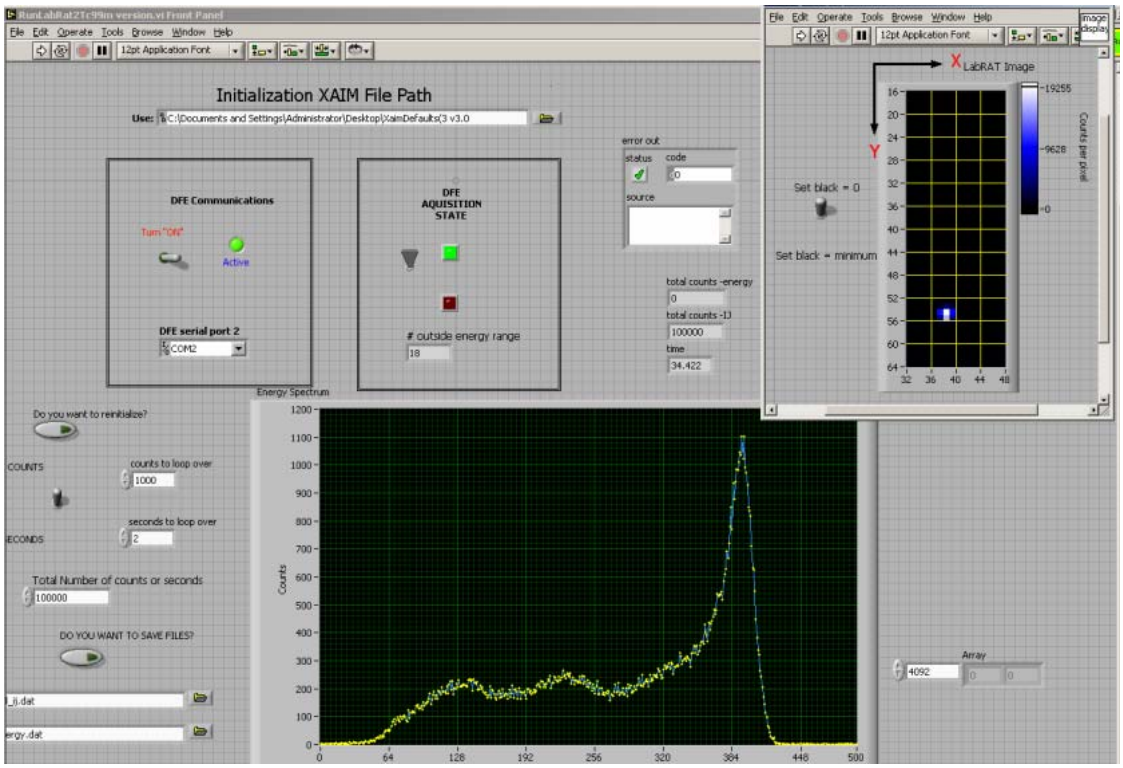

Figure 11. Front panel for the LabRAT system software. Image display is shown in the inset.

3.1 Initialization

The initialization phase of detector operation includes establishing communication between the computer and the detector as well as setting the initialization parameters in the detector electronics and the ASICs. The detector is configured accordingly. Figure 12 shows the front panel for the detector front end (DFE) initialization program. The block diagrams for the DFE initialization are given in Appendix B. The user chooses a configuration file to use, which contains initial input parameters for the detector. Once this file is loaded , the user has the ability to change module-wide, ASIC-wide or individual pixel parameters. The user sets a detector-wide gross threshold on the front panel. The user has the choice of setting the detector to normal operation (detecting gamma ray events) or running the system in calibration mode on a specific pixel. A description of the calibration procedure is given in Chapter 4.

The file that is read in during initialization is called an XAIM defaults file. An example of a part of a defaults file is given in Figure 13. A detailed explanation of each of the parameters in the defaults file is given in Appendix C**.** THE DFESETTINGS entry at the beginning of the file (PILEUPREJECT and DFETHRESHOLD) apply to the entire detector. The rest of the parameters (listed under [ASIC24] in Figure 13) apply to a particular ASIC. A complete defaults file has parameters for each ASIC in use in the detector.

The next major step in the initialization phase of the software is the subVI called MAKEDFEDEFAULTS. The front panel for MAKEDFEDEFAULTS is shown in Figure 14; the block diagram is shown in Appendix B. This program takes default parameters from the input file and allows the user to modify them before the detector is initialized. The arrays of LEDs to disable pixels can be seen, as well as the slider controls to adjust

individual pixel thresholds. All other parameters from the defaults file can be adjusted by the controls in this subVI as well.

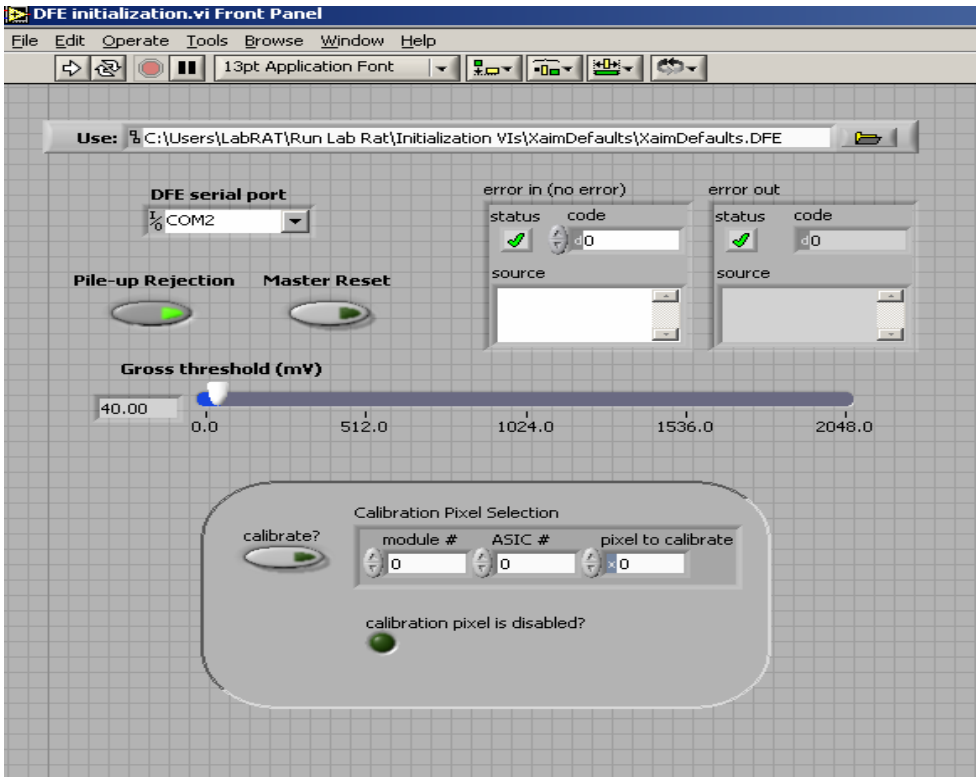

Figure 12. Front panel for the DFE initialization VI.

```
XaimDefaults3b.DFE
[DfeSettings]
PileupReject=TRUE
DfeThreshold=30.000000
[ASIC24]
Version=3.2
BlockLateTriggers=TRUE
DisableCurrentCompensation=FALSE
DisablePixels=0000000000000000000010000010001000000010000000000000000000
00000000000000000000000000000000000000000000000000000000000000000000
AsicThreshold=0
PixelThresholds=03300000000000000000000000000000000000000000000000000000000
00000000000000000000000000000000000000000000000000000000000000000000
MainBias=0
TriggerWidth=0
TriggerDelay=0
ShapingTime=0
PreampFeedback=0
AnalogOutVref=1
TrimDAC=0
```

Figure 13. Part of a LabRAT configuration file.

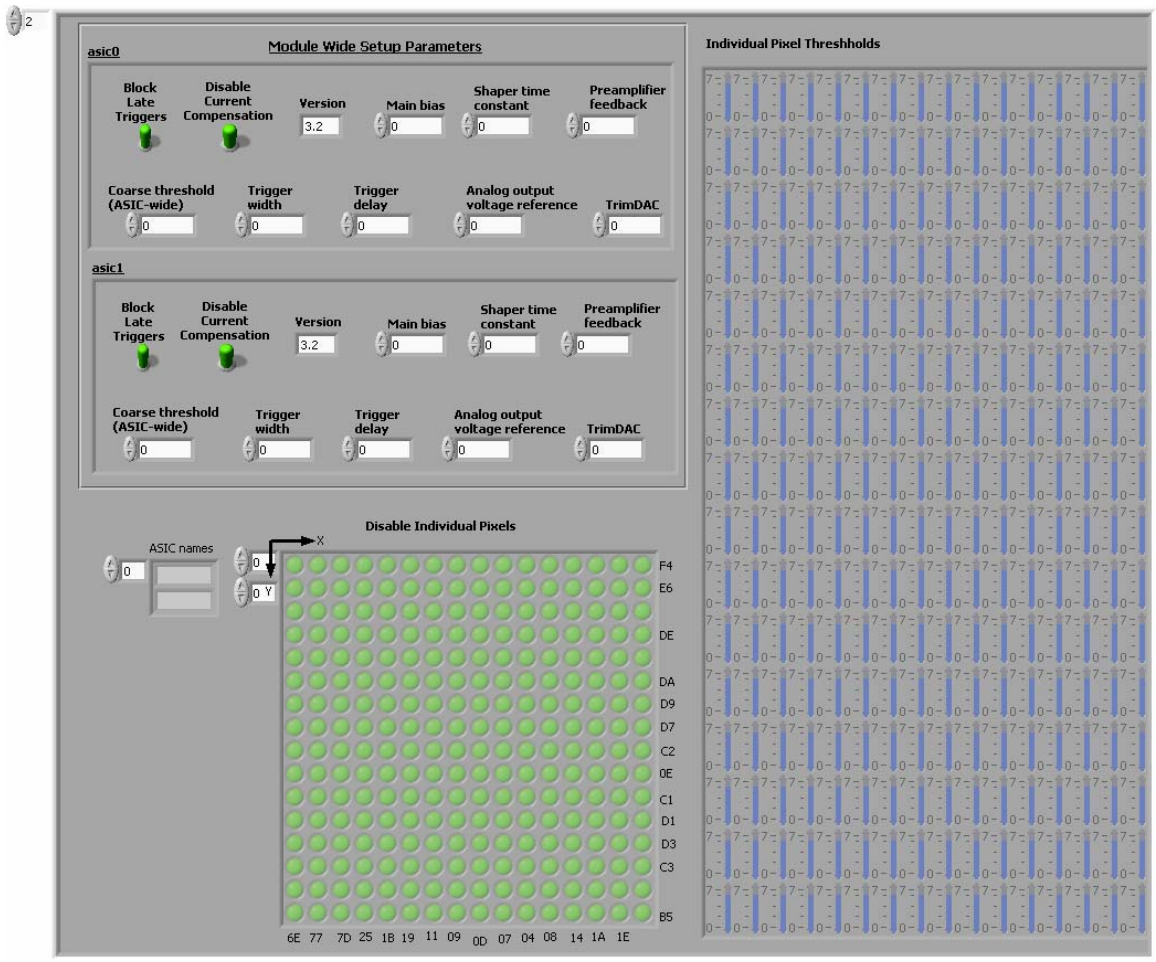

Figure 14. Front panel for the MAKEDFEDEFAULTS program.

3.2 Acquisition

Mosaic Imaging provided a rudimentary data acquisition program, but we rewrote essentially all parts of it. During acquisition, incoming photons interact in the detector modules, creating a current in the CZT which is picked up as a current signal by the ASIC circuitry bonded to each pixel. For each event, two binary numbers are produced containing the energy information and pixel location information. The transfer of this information from detector to computer occurs in the subVI EVENTS2DISK shown in Figure 15; the block diagram is shown in Appendix B. Although the core of

EVENTS2DISK is comparable to that provided by Mosaic Imaging, we added the capability for the program to update the image display and energy spectra during the acquisition and to increase the acquisition speed of the software.

Each radiation interaction event from the detector that is sent to the computer contains two pieces of information: a pixel word encoding the location of the interaction in the detector and an energy word containing the energy information for that event. During acquisition, the two words are read from the detector, then the energy and pixel values are histogrammed into the energy spectrum and image. This histogramming includes checking the energy word to make sure that it is within the energy window and that no errors occured during the acquisition. Each pixel word comprises a seven bit value to specify the pixel within the ASIC, one bit to specify the ASIC within a module, and up to eight additional bits to specify the module within the detector system. The pixel map (see Figure 7) uniquely identifies each pixel in a module. Each module is uniquely identified by its location in the 5 x 5 matrix of detector modules according to the numbering scheme shown in Figure 9. Using the pixel map and module ID, each interaction location is mapped to its (x,y) coordinate for image display.

3.3 Image and Energy Spectra Display

The image and energy spectra display are fairly straightforward once the position and energy outputs have been decoded. The image display front panel is shown in Figure 16; the block diagram is shown in Appendix B. The image display contains a representative square for each pixel in each module of the detector. The total number of photon interactions in each pixel is represented with a color intensity relative to the number of interactions in other pixels. The maximum value of the color scale is mapped

to the pixel with the maximum number of interactions. A control switch maps the minimum value either to zero or to the pixel with the least number of events; however, due to noisy pixels being turned off, there are always zero values. The display window can be sized to show all 5 x 5 modules (or 80 x 80 pixels), or sized to show only specific modules. In Figure 16, the window is sized to show only the three existing modules of LabRAT. An example of an energy spectrum obtained with LabRAT was shown in Figure 4. The energy word values from the detector range from 0-4095, but the energy spectra is histogrammed for display purposes into 512 channels to improve the statistics per channel and the visual appearance of the energy spectrum. The horizontal axis of the energy spectrum in Figure 3 is shown in units of channels, but it can be converted to keV after appropriate calibration.

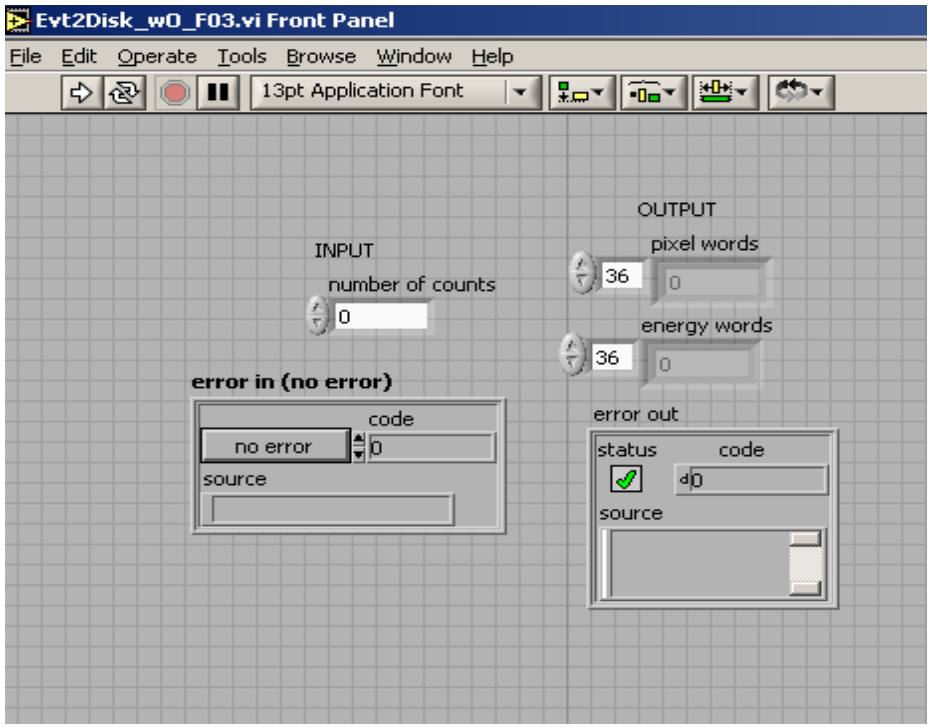

Figure 15. Events2disk acquisition subprogram front panel.

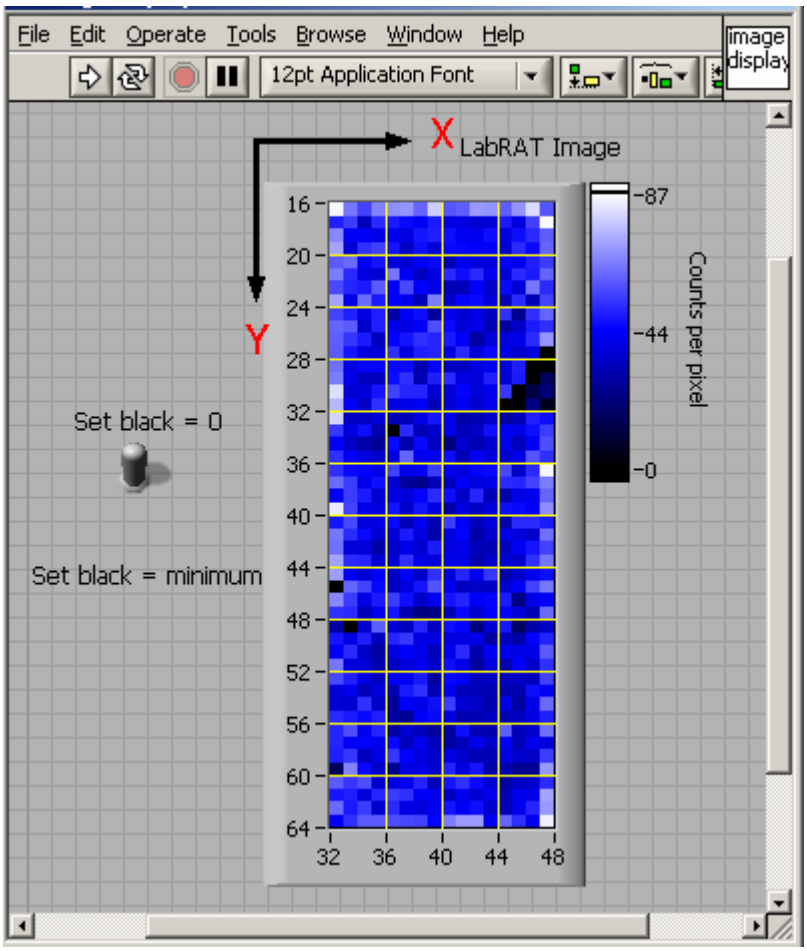

Figure 16. Image display VI showing a flood field acquisition for LabRAT 1. Black squares are pixels that were disabled in the initialization VI.

Chapter 4

Tuning the Detector

Due to the pixelated structure of the detector and inherent inhomogeneities resulting from the fabrication process of the CZT crystals, there can be significant variation in the responses of individual pixels to identical signals. This was apparent immediately after we started obtaining energy spectra for individual pixels from LabRAT. There is variation in the channel in which the peak occurs as well as in the shape of the energy spectrum. The variations between pixels were much less pronounced for LabRAT 0 than for LabRAT 1. Figures 17 and 18 show a representative sample of pixels from each detector. Note the greater uniformity among the pixels for LabRAT 0. The numbers in parentheses above each spectrum are the (x,y) coordinates of the individual pixel in the detector. The larger font number in the upper left hand corner is the channel number where the highest number of counts occurred.

The composite energy spectrum for the whole detector, which is the sum of all the per-pixel spectra, is much wider due to the fact that the photopeak channel is shifting from pixel to pixel, spreading the overall spectrum over the range of peak channels for all pixels. Composite energy spectra for the two LabRAT systems are given in Figures 19 and 20. Energy resolution is a measure of the width of the photopeak expressed as

$$Energy\,Resolution = \left(\frac{FWHM}{Channel\,or\,Energy\,of\;Photopeak\,Centroid} \right) \bullet 100\,\% \quad (1)$$

where

FWHM = the full width at half maximum of the photopeak.

The shifting of photopeak centers widens the peak, resulting in a poorer measured energy resolution than what should be achieved with a well-tuned detector. Energy resolution for LabRAT 1 according to the spectrum in Figure 19 is approximately 60%. Energy resolution for LabRAT 0 according to the spectrum in Figure 20 is approximately 27%. The distribution for LabRAT 0 is much more narrow than that for LabRAT 1 due to greater uniformity in energy response on that detector.

The ASIC design provides a calibration signal. This signal is a voltage pulse added into the preamplifier circuit of individual pixels separately from where the incoming radiation events are gathered. It is created within the ASIC and the user can control the pulse magnitude and the number of pulses. The idea is to insert an artificially uniform pulse and observe how the different pixels respond. With the proper voltage and with the detector-wide threshold set at an appropriate level, it should be easy to produce a sharp, clearly defined calibration peak. It was somewhat surprising to us to find that enabling the calibration pulse produced persistent large noise peaks in the spectra. If the calibration peak overlaps one of the noise peaks, it can become difficult to identify. By changing the voltage level of the calibration pulses, it is possible to move the calibration peak away from the noise peaks, but yet again each pixel responds differently to the identical signal. This makes it very difficult to automate the process of tuning the detector. Months were spent trying to implement an automatic calibration scheme using the ASIC calibration pulses, but in the end it was decided that it was necessary to revert to the cumbersome method of manually calibrating the system by measuring energy spectra with a point source of radiation. Using a motorized translation stage we step the radiation source to the center of each pixel and measure the energy resolution and

photopeak center individually for each pixel. The measured photopeak centers can then be used during imaging to implement per pixel energy windows. These measurements are described in further detail in section 5.2. The ASIC design allows a baseline shift to be applied to all pixel outputs for an ASIC. This initialization parameter, called LS Bias, alters the baseline output voltage positively or negatively based on the value given to LS Bias in the ASIC initialization [10]. Table 1 gives the allowed LS Bias values. LS Bias provides a coarse adjustment to bring the photopeak center channel values into closer agreement.

We set a detector-wide gross threshold that seemed on average to remove the low end electronic noise without cutting off the signal. Then we measured the ASIC baseline voltage offset individually by running flood field acquisitions with a single ASIC turned on and seeing how the composite photopeak channel center changed as we adjusted the baseline voltage offset. The default setting was zero for all ASICs and voltage can be increased positively or negatively from the baseline which is zero volts.

We chose channel 350 for the desired photopeak channel location and adjusted the LS Bias on each ASIC to move its center channel closer to channel 350. Channel 350 was chosen by visually scanning the flood field pixel spectra (such as in Figures 16 and 17) for that ASIC and determining an approximate average for the channel number where the photopeak was occuring.

To complicate matters, the ASICs do not respond uniformly to the choice of LS Bias. For an identical change in LS Bias one ASIC might shift 25 channels while another would shift 40 or more. Table 2 summarizes the effect of LS Bias settings on the

ASICs of LabRAT 1. The pixel response was uniform enough for LabRAT 0 that we only changed the LS bias on one ASIC (ASIC 1 on module 3) by a shift value of one.

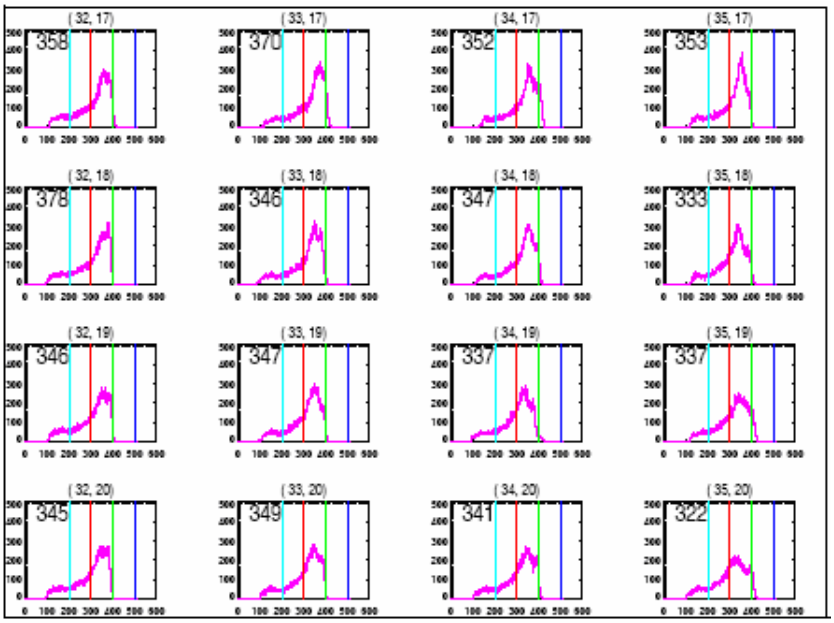

Figure 17. Sample per-pixel energy spectra for LabRAT 1, acquired by flooding the system with 140 keV gamma rays from a point source at 1.5 m distance. The pixel coordinate is noted above each graph and the channel with the most counts is recorded on each spectrum.

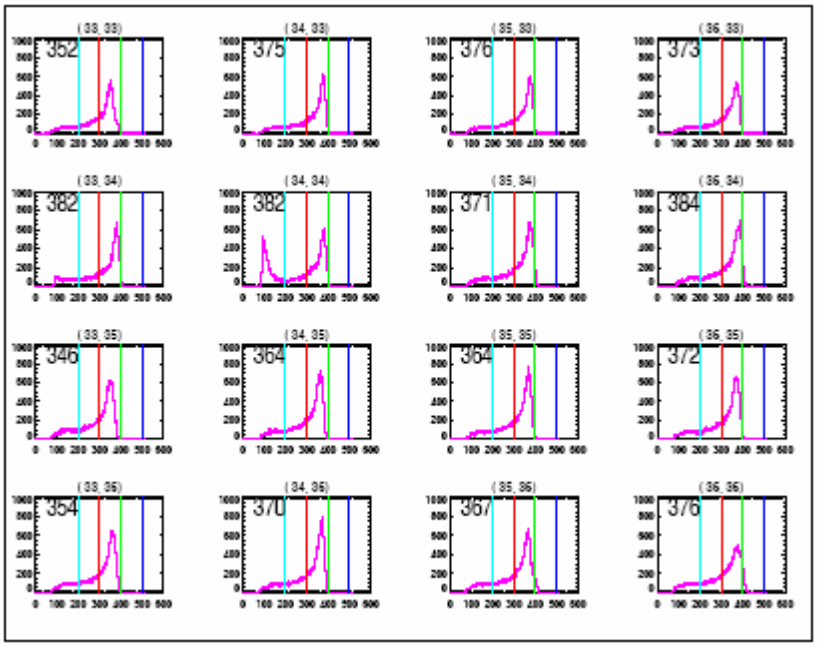

Figure 18. Sample per-pixel energy spectra for LabRAT 0, same measurement conditions as Figure 17.

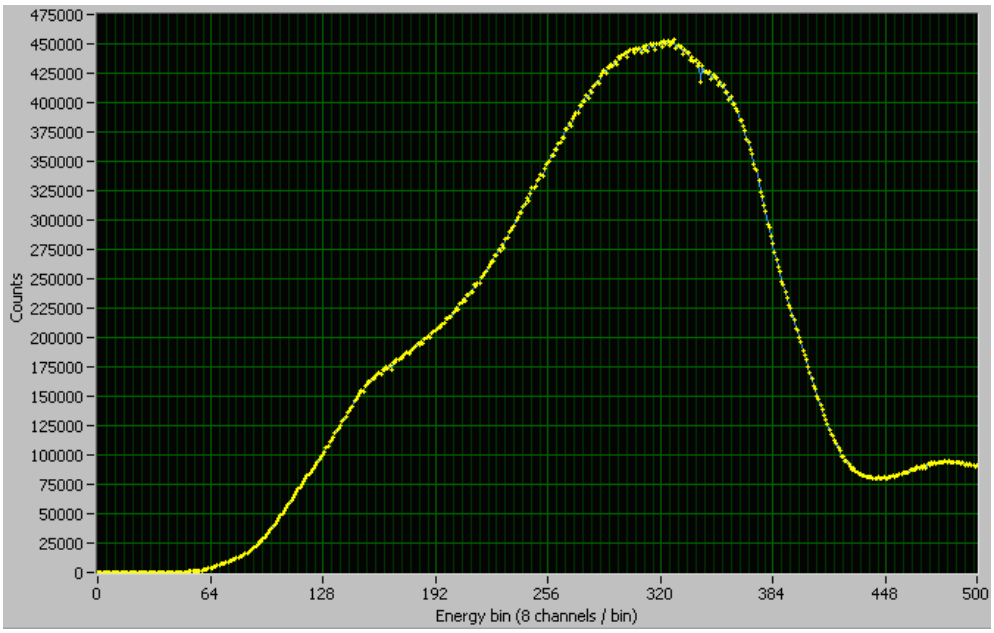

Figure 19. Composite energy spectrum for LabRAT 1, measured with a Tc-99m point source at 1.5 m distance. The spectrum contains ten million counts, default settings were used for all ASIC parameters.

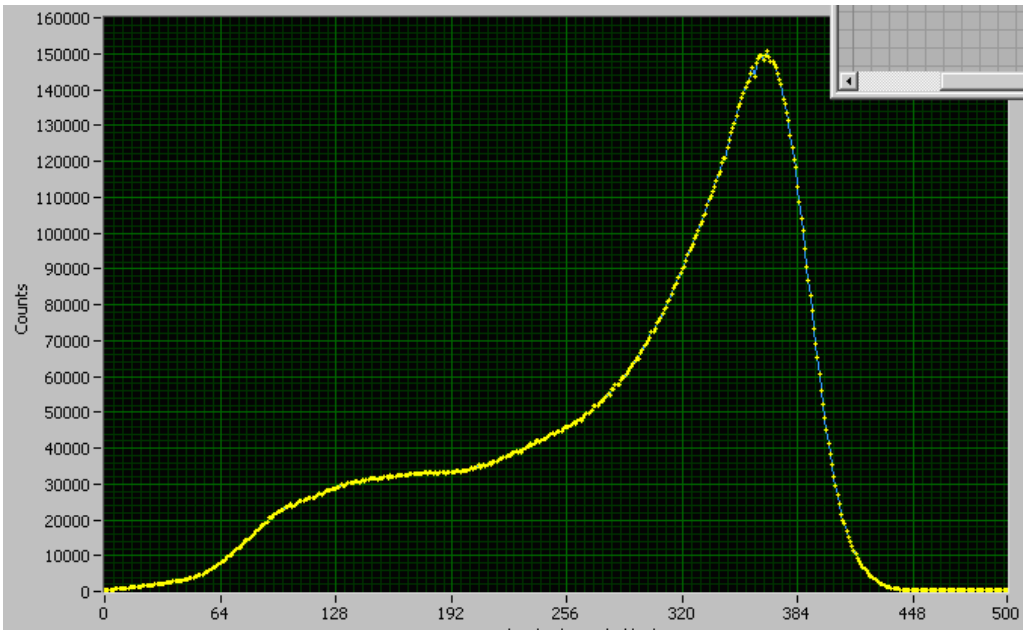

Figure 20. Composite energy spectrum for LabRAT 0, measured with a Tc-99m point source at 1.5 m distance. The spectrum contains ten million counts, default settings were used for all ASIC parameters.

Table 1. Voltage offset values for LS Bias shift.

Shift Value	Offset change (mV)
0	None
1	-15
2	-35
3	-50
4	None
5	15
6	35
7	50

Table 2. Effect of LS Bias setting on the center channel of an ASIC's composite photopeak for LabRAT 1. A Tc-99m point source was used to produce the energy spectra.

Module,ASIC	Shift: Starting LS Bias→Ending LS Bias	Effect of Shift: Starting Center Channel of Photopeak→Ending Center Channel of Photopeak	Final Choice of LS Bias
1,0	0→1	300→340	1
1,0	0→2	300→380	
1,0	0→3	300→420	
1,1	0→1	275→300	3
1,1	0→2	275→320	
1,1	0→3	275→350	
2,0	0→1	350→380	0
2,0	0→2	350→430	
2,0	0→3	350→450	
2,1	0→1	350→390	0
2,1	0→2	350→450	
2,1	0→3	350→500+	
3,0	0→5	380→350	5
3,0	0→6	380→300	
3,0	0→7	380→260	
3,1	0→5	500→475	7
3,1	0→6	500→420	
3,1	0→7	500→400	

We collected flood field energy spectra before the LS Bias changes were implemented and then compared it to energy spectra taken after the changes were made. A Tc-99m source was used and ten million counts were gathered over the entire detector. Table 3 shows the results of the LS Bias changes. The average photopeak channel was calculated from the energy spectra for individual pixels, using the highest- count channel number (i.e., the channels noted on each spectrum in Figures 17 and 18). Figure 21 is the composite energy spectrum for LabRAT 1 acquired after the LS Bias shifts were implemented. The energy resolution according to this spectrum improved from 60% to 40% (compare to Figure 18).

Table 3. Summary of effect of LS Bias settings on the photopeak center channel numbers for LabRAT 1. A Tc-99m source was used.

	Peak Channel Numbers		
	Module 1	**Module 1**	**Module 1**
	ASIC 0	**ASIC 1**	**Module Average**
Default LS Bias Settings	**	**	288
New LS Bias Settings	346 +/- 119	325 +/- 113	336 +/- 116
	Module 2	**Module 2**	**Module 2**
	ASIC 0	**ASIC 1**	**Module Average**
Default LS Bias Settings	**	**	330
New LS Bias Settings	386 +/- 53	367 +/- 52	377 +/- 53
	Module 3	**Module 3**	**Module 3**
	ASIC 0	**ASIC 1**	**Module Average**
Default LS Bias Settings	**	**	414
New LS Bias Settings	372 +/- 65	365 +/- 74	369 +/- 70
	Detector Average		
Default LS Bias Settings	344 +/- 64		
New LS Bias Settings	361 +/- 33		

** Values for individual ASICs were not calculated.

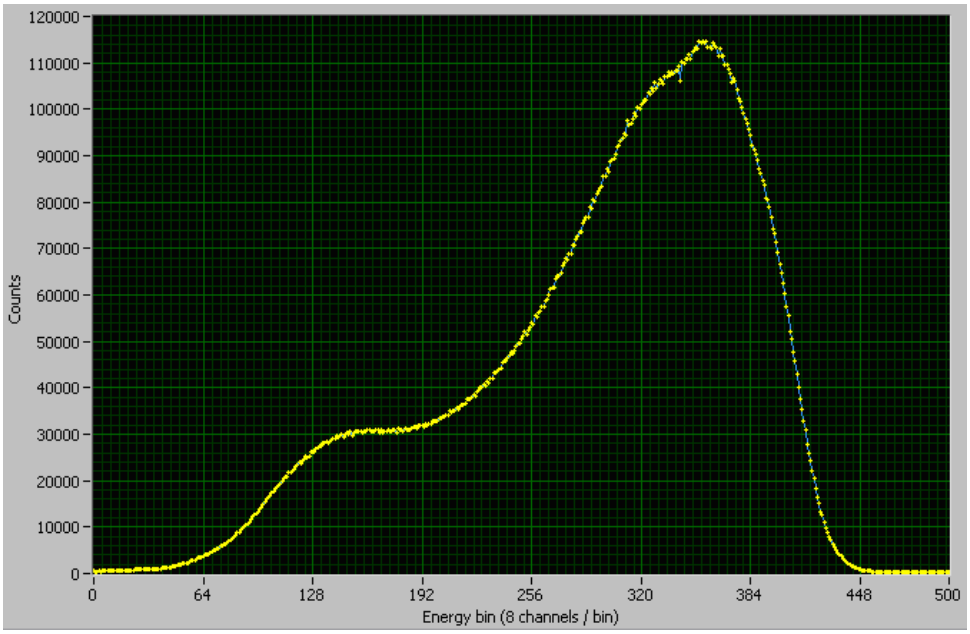

Figure 21. Composite energy spectrum for LabRAT 1 after the LS Bias shifts were implemented. Tc-99m was used as the flood source.

The effect of the LS Bias change for LabRAT 0 is less pronounced than for LabRAT 1, but still apparent. Figure 22 shows flood-field energy spectra from LabRAT 0 for a Ba-133 source before (left) and after (right) changing the LS Bias settings. Figure 23 shows flood-field energy spectra from LabRAT 0 for a Co-57 source before (left) and after (right) changing the LS Bias settings. Table 4 summarizes the effect of the LS Bias shifts on composite energy resolution for LabRAT 0. The effects of tuning are obviously critical for CZT detectors. The ability to apply baseline shifts to individual pixels is highly desirable, but unfortunately is not available with these ASIC designs.

For both LabRAT systems, the peak channel numbers were obtained from composite energy spectra using Tc-99m (140 keV photopeak), Co-57 (122 keV primary photopeak) and Ba-133 (81 keV primary photopeak) sources. Using these values and the known photopeak energies for these radionuclides, an energy calibration curve was

calculated for each system (see Figures 24 and 25). The three data points were fit to a straight line using Microsoft Excel. During imaging, the calibration curve can be used to display energy spectra in terms of keV rather than the more arbitrary value of channel numbers. Because the same software is operating both systems, with slightly different calibration curves, we have typically continued displaying energy spectra in terms of channels

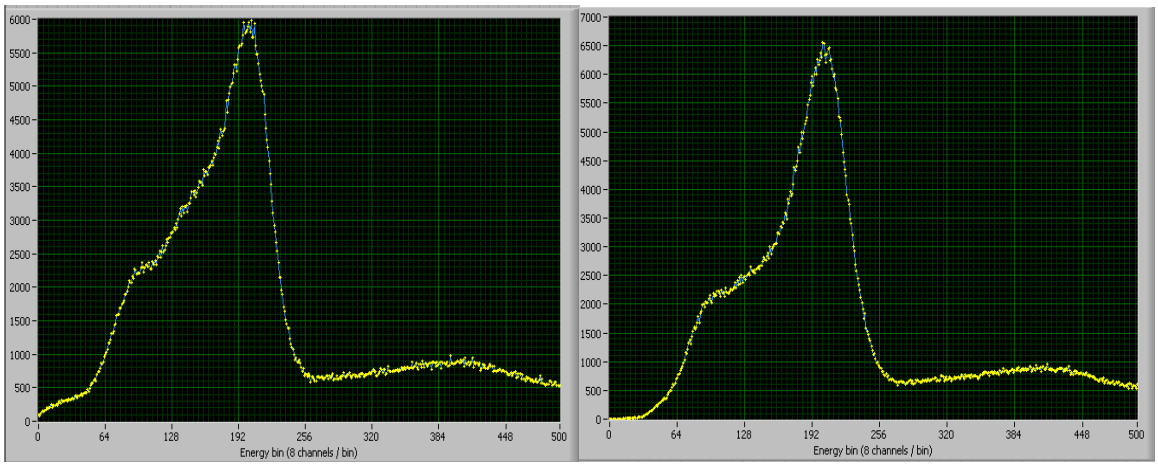

Figure 22. Composite energy spectra for LabRAT 0 with all LS Bias settings at zero (left) and with modified settings (right). The LS Bias of ASIC 1 on module 3 was the only setting changed. A Ba-133 source was used and one million total events were collected.

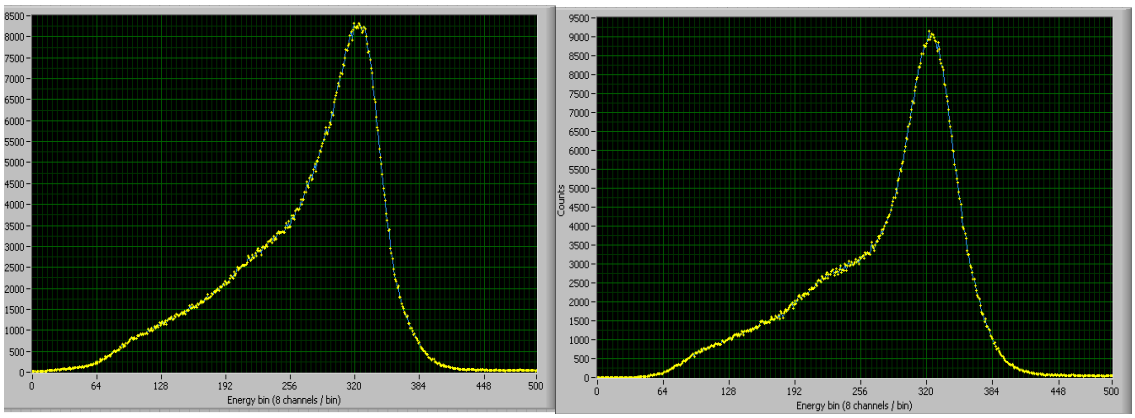

Figure 23. Composite energy spectra for LabRAT 0 with all LS Bias settings at zero (left) and with modified settings (right). The LS Bias of ASIC 1 on module 3 was the only setting changed. A Co-57 source was used and one million total events were collected.

Table 4. Measured energy resolutions for LabRAT 0 before and after implementing the LS bias shifts.

	Energy Resolution (%)	
Flood Source	**Default LS Bias Settings**	**Modified LS Bias Settings**
Ba-133	47%	32%
Co-57	24%	20%

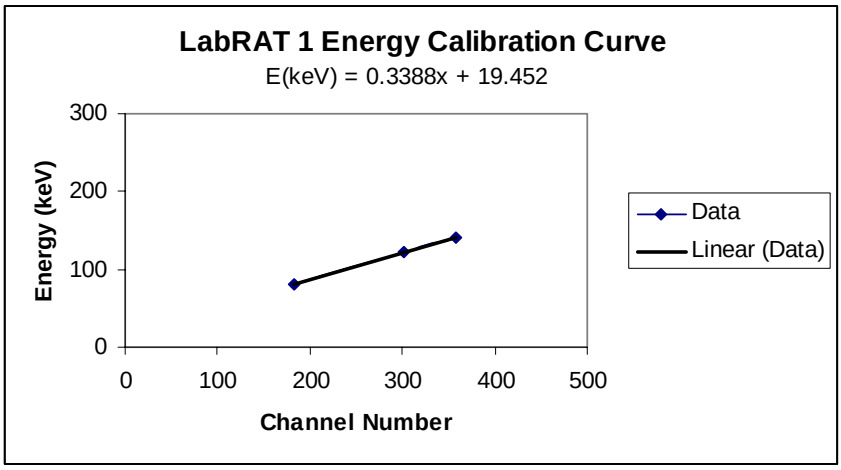

Figure 24. Energy calibration curve for LabRAT 1.

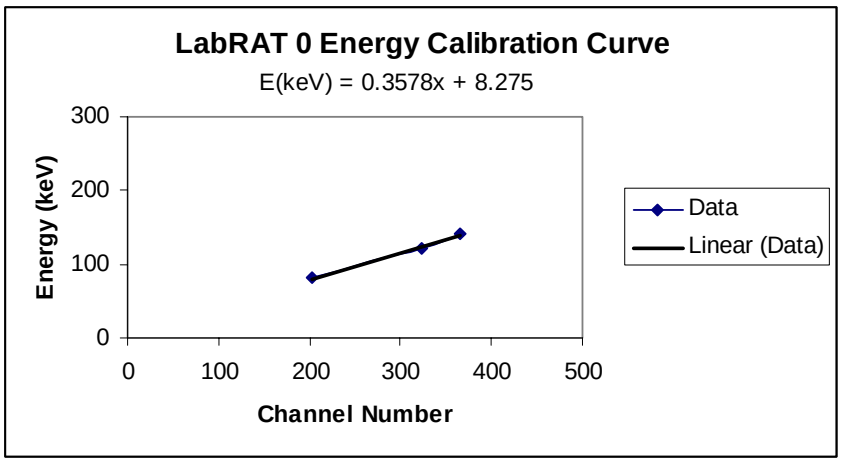

Figure 25. Energy calibration curve for LabRAT 0.

Chapter 5

LabRAT Performance Evaluation

The performance evaluation was done according to National Electrical Manufacturers Association standards [3]. Deviations from these guidelines are noted where appropriate; some tests were modified to acccomodate particular aspects of the LabRAT system or the available types and activities of radioisotopes. The majority of the data analysis was done in IDL 6.1 [25], although some analysis used Microsoft Excel. Five types of tests were performed and a section is devoted to the description and results of each. The tests are

1. Count Rate Performance
2. Energy Resolution and Uniformity of Detector Response
3. Extrinsic Spatial Resolution
4. Linearity
5. Integral and Differential Uniformity

These tests highlight the most fundamental aspects of intrinsic detector performance and some aspects of system performance, but do not cover the full gamut of acceptance testing normally applied to a nuclear medicine imaging system. In particular, without a dedicated collimator, some extrinsic and tomographic tests could not reasonably be performed.

5.1 Count Rate Performance

The primary radionuclide used for this test was Tc-99m; Ba-133 was also used for some count rate measurements. The Tc-99m was placed in a plugged syringe cap (see Figure 26) wrapped in gauze and wedged into the middle of the length of the holder so it would stay in place. An illustration of the source geometry is given in Figure 27 and pictures of the setups for both detectors are given in Figures 28 and 29. NEMA specifies that the distance between source and detector be at least 5 times the maximum dimension of the useful field of view (UFOV). On a scintillation crystal gamma camera, a margin around the outside edge of the crystal is not usable, so the UFOV is smaller than the detector dimensions. With CZT the entire surface of the module is part of the field of view (FOV). Some authors have noted a tendency for edge pixels to respond differently than other pixels. Wagenaar states that "pixels located on the edges and especially the corners of the square arrays generally are less responsive than internal pixels" [6]. In our measurements, we did not notice a distinct enough pattern of response to systematically correct for edge effects. The FOV for LabRAT 1 is 38.4 mm x 117.6 mm (38.4 mm for each of three modules plus 1.2 mm gaps between modules). The FOV for LabRAT 0 with its two modules is 38.4 mm x 78 mm. As long as the source-detector distance is at least 58.8 cm, the NEMA criterion is satisfied for both detectors. We used 100 cm and 150 cm distances for the count rate tests.

Ten-million and twenty-million count flood fields were acquired for the two systems; the energy and pixel locations of each interaction were saved in list-mode by the LabRAT acquisition software. Programs were written in IDL to read the data from the

file, sort it by pixel and construct an energy spectrum for each pixel. These data were used for tuning the detector, described in Chapter 4, and shown in part in Figures 17 and 18.

Figure 26. Syringe caps used to hold Tc-99m.

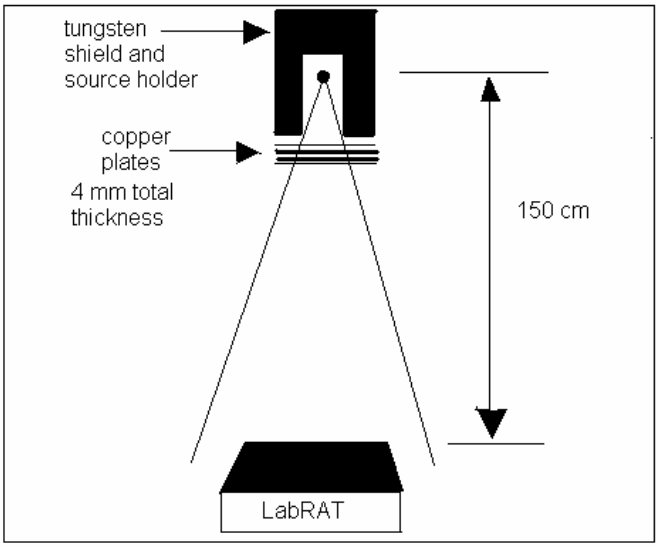

Figure 27. Source and detector geometry for count rate measurements.

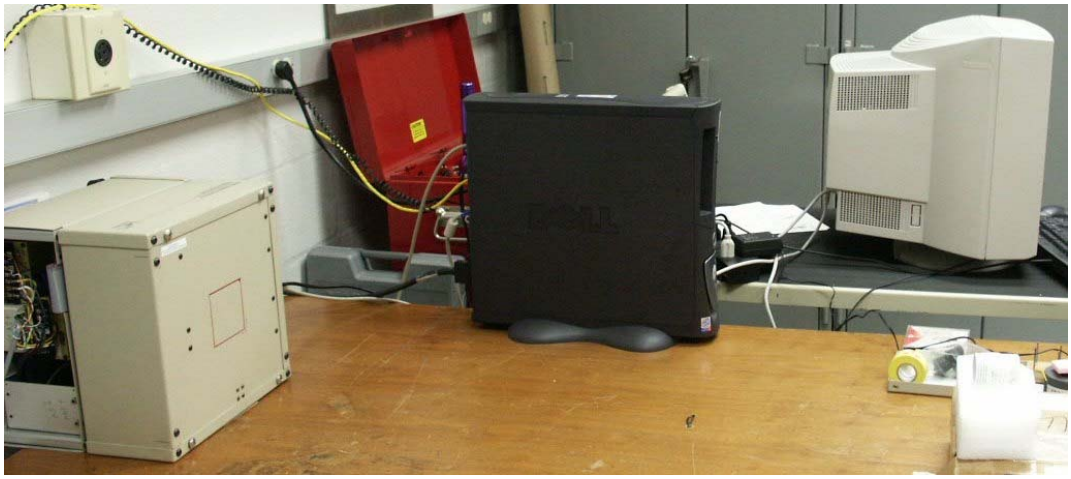

Figure 28. Photograph of Labrat 1 count rate setup. LabRAT 1 is at the far left and the acquisition computer is in the background; the tungsten source holder is at the far right on the white block.

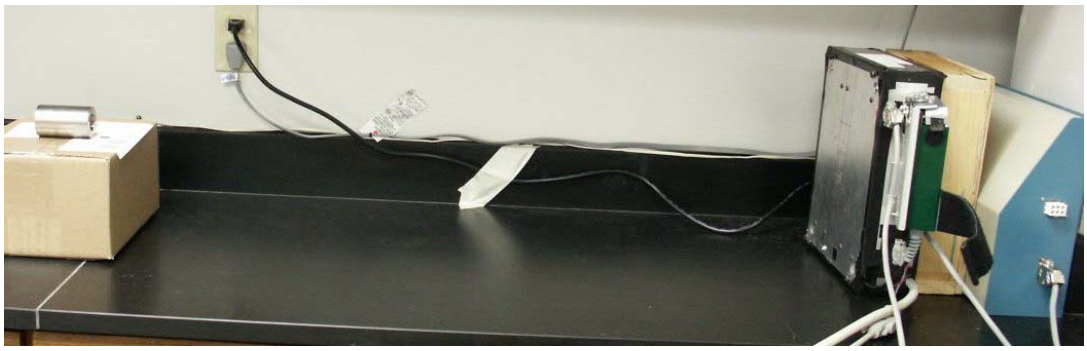

Figure 29. Photograph of LabRAT 0 count rate setup. LabRAT 0 is on the far-right. The tungsten source holder is on the far-left on the box. The copper plates have not yet been placed over the end of the holder.

The idea behind the count rate tests is to measure the "observed count rate for a 20% count loss and a maximum count rate" [3]. We started with 16.5 mCi of Tc-99m for one acquisition with LabRAT 1, with 2.34 mCi of Tc-99m for one acquisition with LabRAT 0, and with a 7.77 mCi Tc-99m source positioned equidistant between both detectors for yet another acquisition.

The count rate at the face of a LabRAT system from a Tc-99m source is given approximately by

$$C = A \cdot Y \cdot \Omega(a,d) \cdot \varepsilon(5\,mm, 140\,keV) \quad (2)$$

where

C = count rate at detector (counts/sec)
A = source activity (disintegrations/sec)
Y = yield (0.89 gammas/disintegration)
$\Omega(a,d)$ = solid angle subtended by detector of area a at distance d
$\varepsilon(5\,mm, 140\,keV)$ = absorption efficiency of detector, ~88% for 5 mm of CZT at 140 keV

Thus,

$$C\,(cps) = A(mCi) \cdot 5.69 \times 10^4 \,{}^{cps}\!/_{mCi} \quad \text{(for 150 cm distance)} \quad (3)$$

and

$$C\,(cps) = A(mCi) \cdot 1.28 \times 10^5 \,{}^{cps}\!/_{mCi} \quad \text{(for 100 cm distance)} \quad (4)$$

For the 16.5 mCi source at 150 cm from the detector, the count rate should have started out at approximately 98,000 counts per second. For the 7.7 mCi source at 100 cm the count rate should have started around 103,000 counts per second.

Imarad's documentation obtained with the CZT modules indicates that the detector acquisition board (DAB) can process 1 million events per second [17]. The DAB converts current based detector outputs to voltage signals which are then stored in digital memory. Both of the detectors demonstrated a count rate maximum around 3300-3500 counts per second! Figures 30 and 31 show the count rate vs. activity for both detectors.

We could not obtain accurate measurements of the maximum count rate and 20% count loss from these measurements because of the abrupt saturation at 3300-3500 counts per second. Attempts were made to reconfigure the acquisition loops and to remove any extra tasks that might restrict the count rate; so far, none of these attempts have solved the problem.

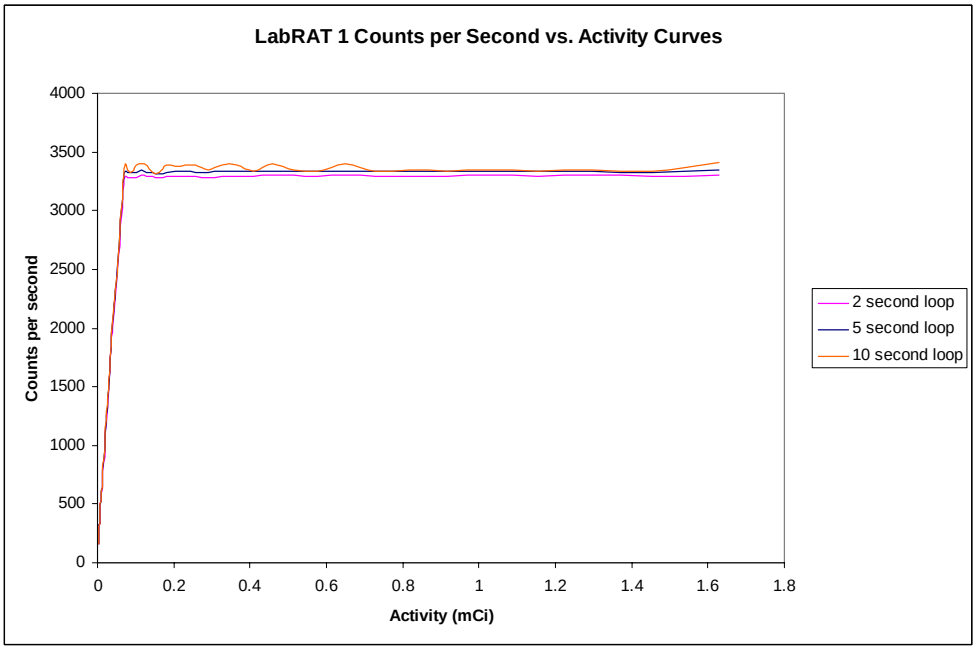

Figure 30. Count rate vs. activity for LabRAT 1. The curves are linear as expected at low activities, then saturate at 3300 count per second. The 2-second, 5-second and 10-second loops indicate the frequency at which the detector updates the image display.

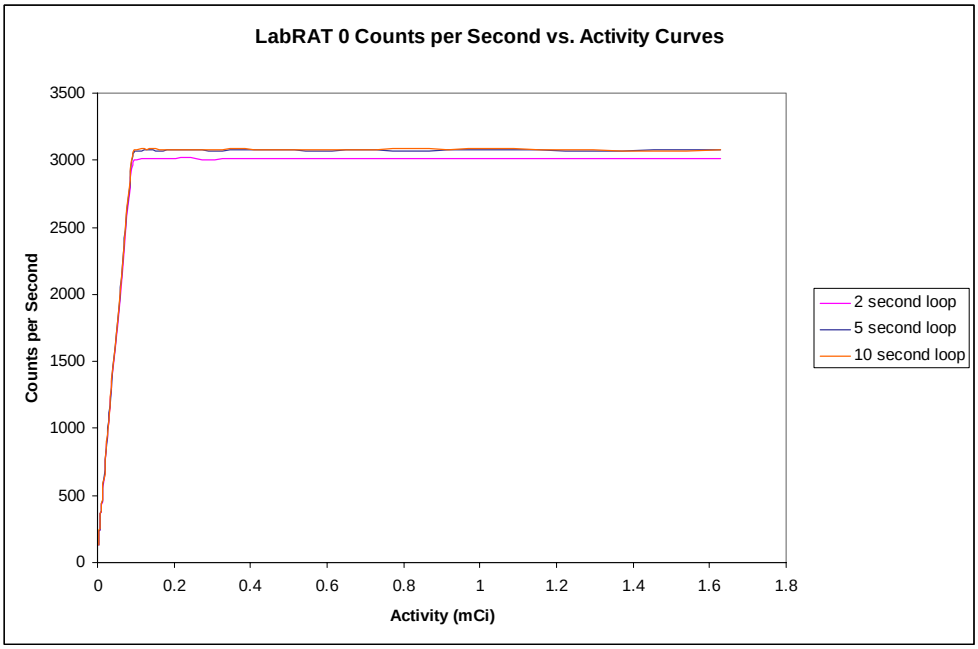

Figure 31. Count rate vs. activity for LabRAT 0. The curves resemble those in Figure 29 for LabRAT 1, except the count rate saturates at 3100 counts per second.

Using an 8 μCi Ba-133 source, a Tektronix TDS 5054 digital phosphour oscilloscope, an Ortec 551 timing single channel analyzer and an Ortec 871 timer/counter we measured the rate of trigger signals directly from the detector data cable. A background count rate reading from LabRAT 1 of 74 cps had been obtained using the LabRAT acquisition program. From the direct trigger signal measurements, a comparable background count rate of 70 cps was measured.

For the Ba-133 source an average count rate of 60,000 cps was measured from the trigger signals. This suggests that the detector hardware is capable of higher count rates than those measured with the LabRAT software and that the restricting factor has been narrowed down to the National Instruments acquisition cards and/or the LabRAT software. Solving the count rate problem is an important issue still to be resolved for the LabRAT system.

5.2 Energy Resolution and Uniformity of Detector Response

This section describes measurements using a collimated radioactive point source scanned over the face of the detector. The radionuclide used for these measurements was Tc-99m sealed in a syringe cap (see Figure 26). The collimated tungsten source holder is shown in Figure 32. The source holder has a series of tungsten discs that can be placed on the holder to collimate the beam to a 1 mm diameter. Three to five collimating discs were used, depending on the activity of the Tc-99m source. The tip of the collimator was placed as close as possible to the detector face, to minimize divergence of the photon beam between the collimator and detector. We placed our source approximately 5 mm from the detector face to assure minimal divergence of the photons after exiting the source holder and adequate total counts at each position.

For the spatial resolution and uniformity of response acquisitions we used a Velmex MaXY motorized translation stage with an NF90 motor controller [26]. The stage's stepper motors are capable of positioning the source holder with precision movement in steps as small as 0.005 mm across the (x,y) plane of the detector. We added a custom frame to the translation stage to hold the detector during the measurements. The frame, translation stage and LabRAT 0 are shown in Figure 33; the LabRAT system mounts "detector-down" over the translation stage and source holder.

A derivative version of the LabRAT software was created for use with the scanning stage; this augmented software integrates the translation stage drivers into the acquisition program. The output list-mode data format was modified to record the motor positions and acquisition start time, in addition to the energy and pixel location information. LabView VIs and a driver library were provided by Velmex with the NF90 motor controller.

5.2.1 Energy Resolution

To measure an accurate energy resolution value for each pixel, the source was stepped across the plane of the detector so that energy spectra were obtained at the center of each pixel for 15 seconds per pixel. The resulting data were decay corrected. To obtain the energy resolution measurements reported in Chapter 4, we measured the FWHM directly from the composite energy spectrum. This is not a feasible approach for per-pixel energy spectra because there is an exponential tail on the low energy side of the photopeak [4] (see Figure 4). A proposed method for measuring energy resolution for CZT energy spectra is to measure the half width at half maximum from the high-energy side of the photopeak and double the value to get the FWHM [27].

Narita et al. [19] recommend fitting the spectra to a combined Gaussian and exponential function to accommodate the two parts of the CZT energy spectrum. A non-linear least-squares routine was written in IDL to implement fitting of CZT energy spectra to the function

$$f(x) = A_0 \exp\left[-\frac{(2.35)^2 (x - A_1)^2}{2A_2^2} \right] + A_3 \exp\left[-A_4 (A_5 - x) \right], \quad \text{for } x \le A_5$$
$$f(x) = A_0 \exp\left[-\frac{(2.35)^2 (x - A_1)^2}{2A_2^2} \right], \quad \text{for } x > A_5 \tag{5}$$

where A_0 = amplitude of Gaussian term

A_1 = center of Gaussian term

A_2 = width (FWHM) of the Gaussian term

A_3 = magnitude of the exponential term

A_4 = decay factor of the exponential term

A_5 = coordinate where exponential term is equal to A_3

Figures 34 and 35 show the results of this curve fitting for the same pixel data, but using different initial input parameters. Curve-fitting routines are notoriously sensitive to the choice of initial fitting parameters. While the fit in Figure 35 is not perfect, the Gaussian term appears to be in good agreement with the high-energy side of the photopeak and the first part of the low-energy side of the photopeak. The calculated energy resolution for this pixel for the fit in Figure 34 is 1.81%, but 6.01% for the fit in Figure 35. For the majority of pixels the fits were visually better than that in Figure 34 and we were able to automate the curve fitting and obtain acceptable curve fits and

energy resolution values. Figure 36 shows a representative sample of pixels that were suitable for automated curve fitting.

Figure 32. Tungsten source holder and collimator discs used for spatial resolution and uniformity of response measurements.

Figure 33. Point source scanning system with detector frame and point source holder. LabRAT 0 is in place on the frame.

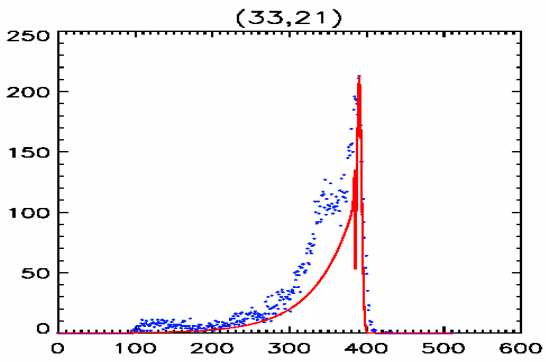

Figure 34. Energy spectrum obtained for a single pixel measured with the scanning source setup. Blue dots shows measured data, red line shows the Gaussian plus exponential curve.

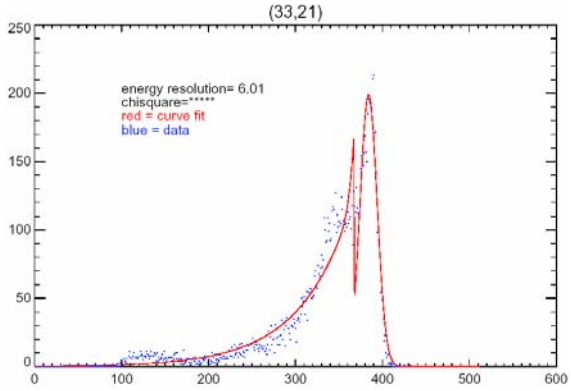

Figure 35. Energy spectrum for the same pixel as in Figure 33, calculated with different initial input parameters to the curve fitting routine. The measured data are blue dots, the red line is the fitted function.

For a handful of pixels, we ran the curve fit routine individually (the pixel in Figures 34 and 35 is such an example). Pixels with an automated energy resolution fit of less than 5% or greater than 10% were re-checked by hand. For some pixels, we were able to obtain a "better" fit by changing the input parameters; for others the data was so irregular (possibly due to scattering or excess charge-cloud sharing with neighboring pixels) that a reasonable fit could not be obtained. "Better" was defined as a visually satisfactory fit of the Gaussian term to the data and an overall chi-squared value for the fit that is comparable to that for similar choices of the initial fit parameters.

Table 5 shows, for both LabRAT systems, the total number of pixels enabled in each module (the other pixels had been disabled during ASIC initialization because they were excessively noisy or dead), the total number of pixels that did not produce usable fits to the spectra, the total number of pixels that had to be analyzed individually and the average per-pixel energy resolution for each module. The overall average per-pixel energy resolution for LabRAT 0 is (7.0 +/- 2.51) % and for LabRAT 1 is (6.48 +/- 2.49)% (compare this to the composite energy resolutions of 27% and 40% respectively for LabRAT 0 and LabRAT 1 reported in Chapter 4). The percentage of pixels with an energy resolution less than or equal to 7% is 72.4% for LabRAT 1 and 58.7% for the LabRAT 0. Again, note that the energy resolutions are measured at 140 keV. Graphical plots of the per-pixel FWHM energy resolution as a function of (x,y) position in the detector are shown in Figure 37.

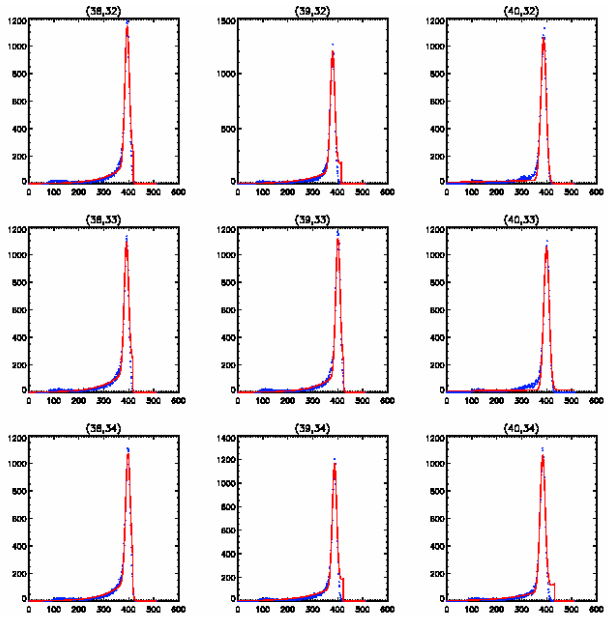

Figure 36. Representative sample of pixel spectra from module 2 of LabRAT 0 for which the Gaussian plus exponential curve fitting routine produced an adequate fit using automated input parameters. Blue dots are measured data; the red line is the fitted function.

Table 5. Curve fitting and energy resolution data for each module in both LabRAT systems.

	LabRAT 1			LabRAT 0	
	Mod. 1	**Mod. 2**	**Mod. 3**	**Mod. 2**	**Mod. 3**
Total Enabled Pixels	249	254	256	251	256
Total Unfit Pixels **	17	9	5	5	5
% Unfit Pixels	6.8	3.5	2	2	2
Total Pixels Fit Individually	60	41	6	1	3
% Pixels Individually Fit	24.1	16.1	2.3	0.4	1.2
Ave. Per-Pixel Energy Resolution (%)	6.28 +/- 2.28	6.11 +/ 1.6	7.04 +/- 2.16	6.49 +/- 1.3	7.44 +/- 2.15

** This number includes four pixels per module that were subsequently identified as being cross-wired (see section 6.1).

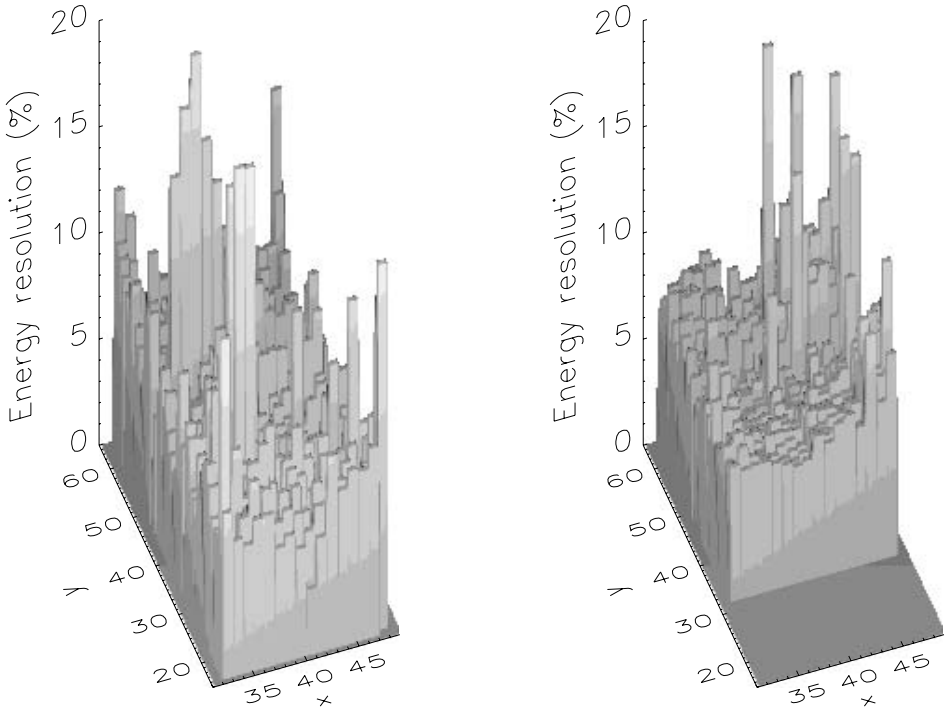

Figure 37. Two dimensional bar plots of per-pixel FWHM energy resolution for LabRAT 1 (left) and LabRAT 0 (right).

.

Subsequent to this analysis, a pair of pixels in each ASIC (four pixels per module) were identified as being cross-wired, but still functional, rather than unfit or dead. Due to

an error in the ASIC layout in the pixel bonding pattern, or simply in the ASIC documentation, the events in each pixel of the pair are mis-assigned to the other pixel. Events and energy spectra for these pixels can be recovered if the pixel data are swapped in the software. This reduces the number of unfit pixels by four for each module. These miswired pixels are discussed further in Chapter 6.

5.2.2 Uniformity of Detector Response

For the uniformity of detector response measurements the source was stepped in 0.4 mm increments along a profile across the length of the detector (across all modules). Each measurement was acquired for fifteen seconds and the resulting data was decay corrected. The data was sorted to group the gamma interaction events that occured in each pixel as the source moved across the detector. Figures 38 and 39 show the response profiles for LabRAT 1 and LabRat 0. The uniformity of response is acceptable for both systems, with the expected dips in the profile at the gaps between modules; the 1.2 mm gap between modules is clearly seen in the profiles for both detectors. On the profile for LabRAT 0 there appear to be dips between the ASICs as well. The slight fluctuation in the response curve is likely due to the position dependent amount of charge sharing between pixels and inherent heterogeneity in charge trapping and collection efficiency.

Individual pixel responses for representative adjacent pixels are shown for the two LabRAT systems in Figures 40 and 41. These curves illustrate how the response of a pixel increases as the source steps into a pixel and reaches a maximum when the source is under the pixel center. The response then decreases as the source moves away from the center, reaching a minimum when the source is over the boundary between pixels. The overlap of the curves for the two pixels demonstrates the phenomenon of charge-sharing

between adjacent pixels. Note that only neighboring pixels share events; pixels that are even one pixel apart from each other show essentially no overlap.

It is also interesting to visualize how the counts acquired by individual pixels vary as the source scans along the row of pixels, crossing from pixel to pixel. It is expected that, due to charge sharing near the boundaries, the acquired counts will be systematically lower near the borders between pixels and greater toward the centers. Figures 42 and 43 show a series of representative images demonstrating this behavior for LabRAT 1 and LabRAT 0, respectively. Each surface represents the total counts (z axis) accumulated in each pixel (x,y) of the detector at the specified relative motor position. Each motor position is noted above the corresponding surface. The zero position was arbitrarily chosen to be at the center of a pixel; six steps (2.4 mm) from this is the center of the next pixel.

5.3 Extrinsic Spatial Resolution

For this test a 1 mm diameter capillary tube was filled with 0.9 mCi Tc-99m; a 4 cm length of the tube contained radioactivity. Although NEMA specifies extrinsic resolution measured at 10 cm from the collimator, we measured the resolution at 5 cm to ensure that the image was contained within the FOV (to facilitate measuring the width of the capillary tube image). An 11 cm x 7 cm x 2.3 cm piece of low-energy, all-purpose parallel hole collimator was placed over the detector. Lead sheet is positioned around the edges of the collimator to shield against side scatter. The capillary tube was held parallel to the detector face at a distance of 5 cm above the face of the collimator. Images were acquired with the capillary tube oriented diagonally, vertically and horizontally with respect to the (x,y) coordinate system of the detector. The detector

setup is shown in Figure 44, the collimator is shown in Figure 45, and Figure 46 shows a sample image acquired for the diagonal orientation with LabRAT 0 with the windowed image on the left and the image without the energy window applied shown on the right.

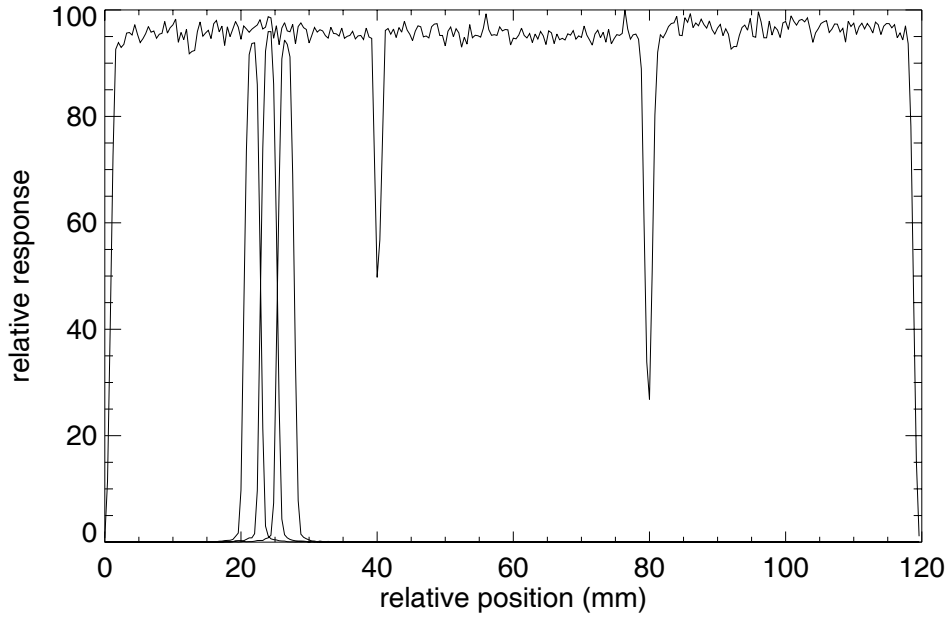

Figure 38. Uniformity profile along the y-direction at x = 37 for LabRAT 1. Dips in the curve near 40 mm and 80 mm show the 1.2 mm gap between modules. Dips at the beginning and end are where the source was beyond the edges of the detector. Three individual pixel response profiles are shown for reference (see Figure 40). Each ASIC in a module contributes to about half of the width of that module's profile.

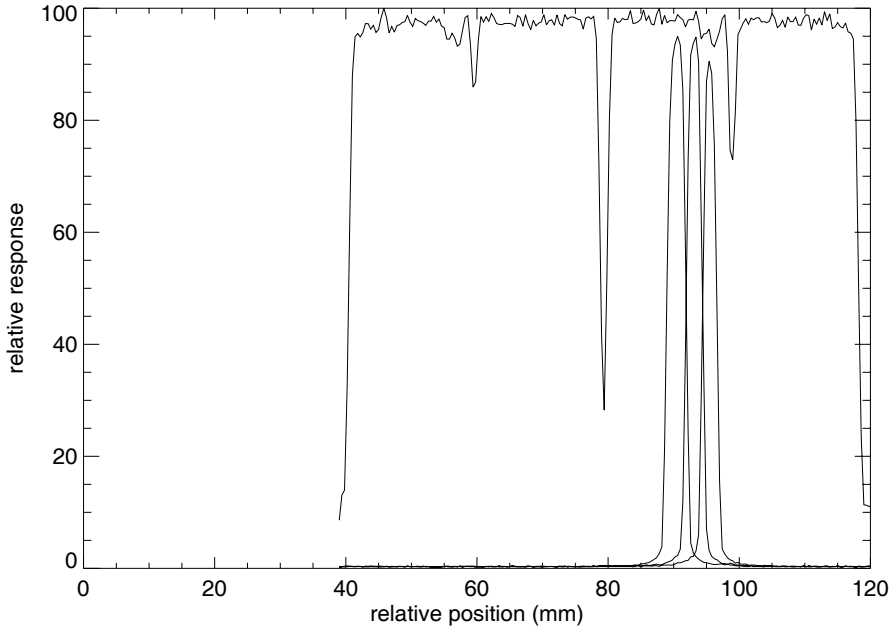

Figure 39. Uniformity profile along the y-direction at x = 39 for LabRAT 0. The dip in the curve near 40 mm shows the 1.2 mm gap between modules. Three individual pixel response curves are shown for reference (see Figure 41).

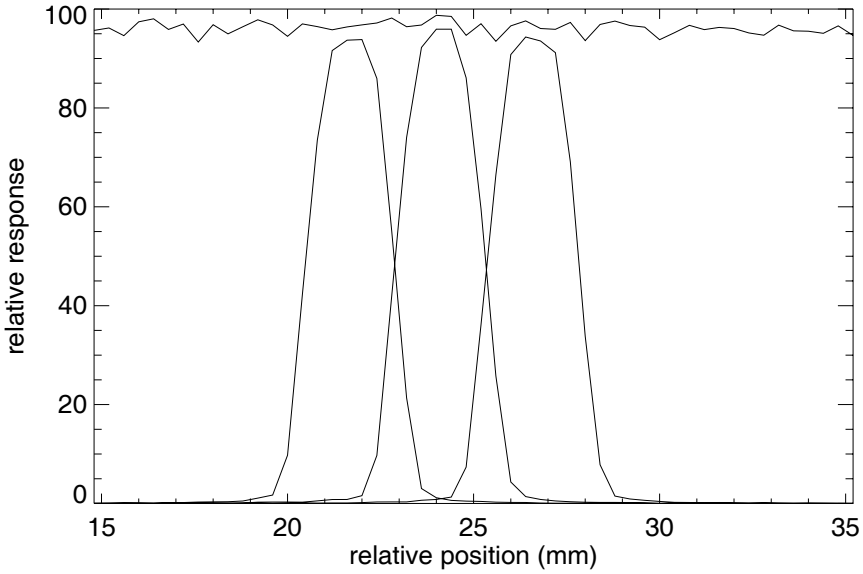

Figure 40. Detail of detector response curve and three individual pixel profiles for LabRAT 1. The responses of adjacent pixels overlap because of charge-sharing between pixels. The overall detector response is the sum of all individual pixel responses.

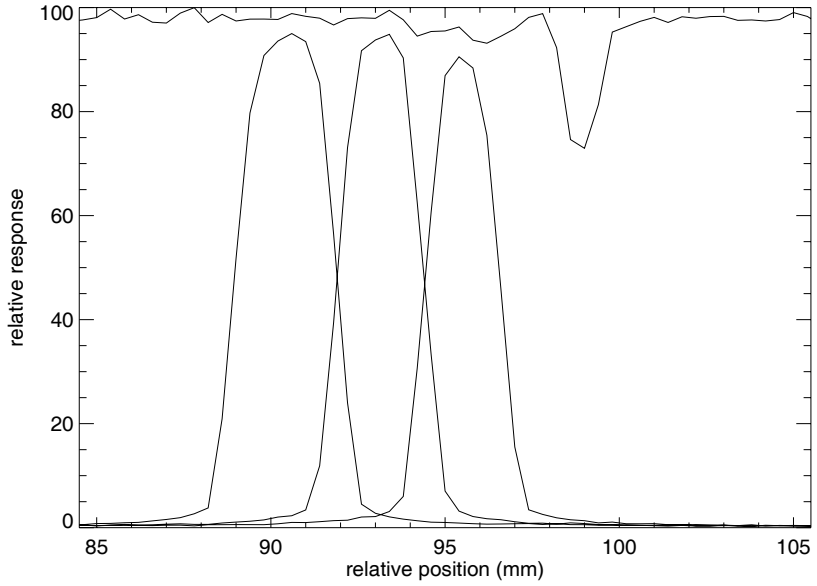

Figure 41. Detail of detector response curve and three individual pixel profiles for LabRAT 0. The responses of adjacent pixels overlap because of charge-sharing between pixels. The overall detector response is the sum of all individual pixel responses

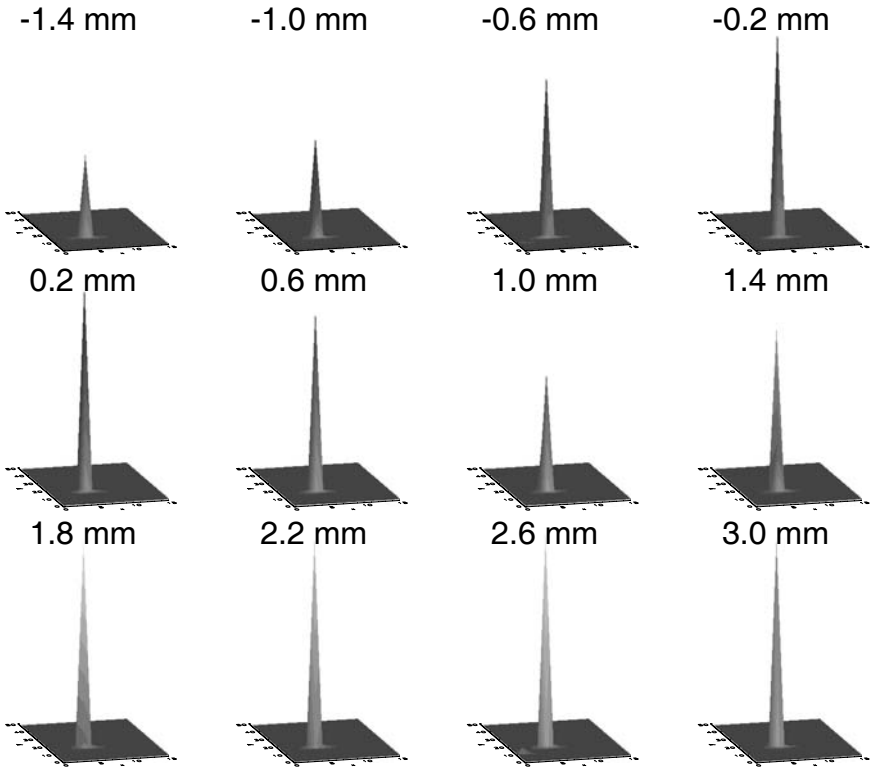

Figure 42. Total counts acquired in all pixels as a function of motor position LabRAT 1. The zero position is the center of a pixel; the twelve surfaces span a range representing two full pixels.

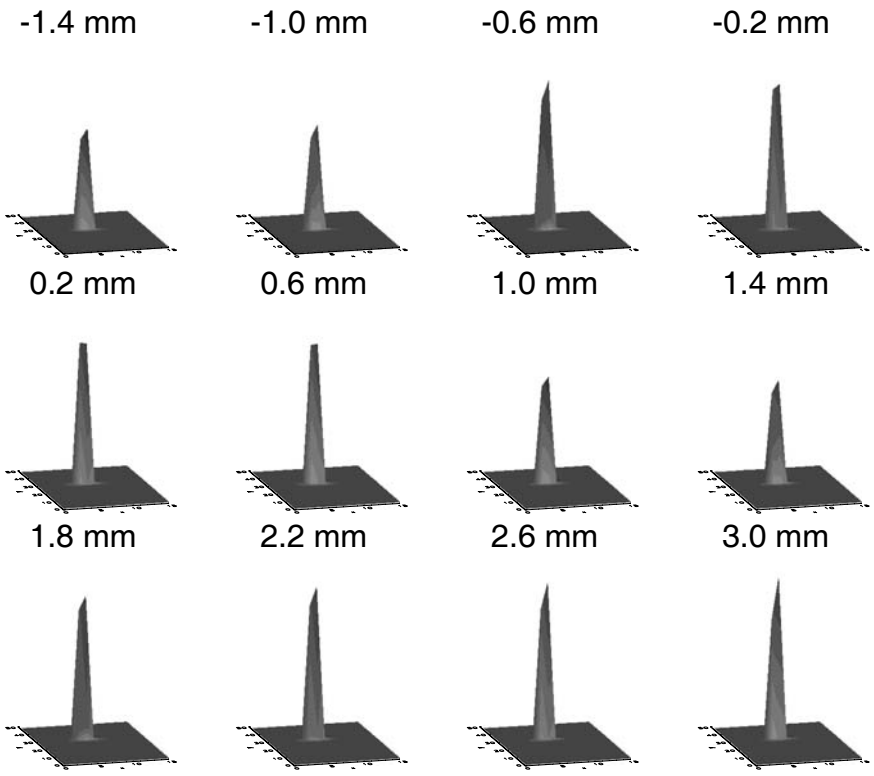

Figure 43. Total counts acquired in all pixels as a function of motor position LabRAT 0. The zero position is the center of one pixel; the twelve surfaces span a range representing two full pixels.

Figure 44. Photograph of experimental setup for measuring extrinsic spatial resolution. The capillary tube is positioned parallel to and 5 cm above the collimator face. Lead sheet around the collimator provides lateral shielding.

Figure 45. Photograph of the low-energy, all-purpose collimator used for extrinsic spatial resolution and uniformity measurements. This piece of collimator is a lead-foil, hexagonal hole design from a Siemens' LEAP collimator.

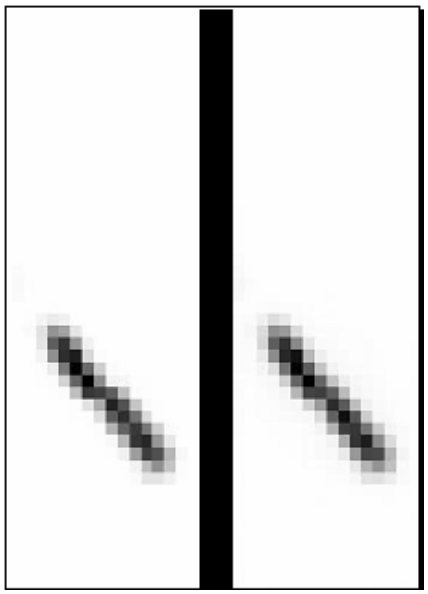

Figure 46. Image of a 1 mm diameter capillary tube at 5 cm distance oriented diagonally, acquired with LabRAT 0.

The measurement of interest in this test is the extrinsic spatial resolution of the system; extrinsic resolution is the combination of collimator resolution and intrinsic detector spatial resolution. A 15% energy window was applied pixel-by-pixel to the data

using the per-pixel fitted photopeak centers (parameter A_1 of equation 5) obtained from the energy resolution measurements of section 5.2.1. For the horizontal and vertical orientations, profiles of the pixels across the axis of the capillary tube were obtained. When dead pixels were present in the images, the average value of the eight pixels surrounding the dead pixel were used for the dead pixel. Each profile was fit to a Gaussian function and the average FWHM of the profiles was calculated for each orientation. Table 6 gives the results. Figures 47 and 48 are representative images for each orientation, both without and with the energy window applied for comparison, for both LabRAT systems. In these figures the windowed image is on the left and the unwindowed image is on the right.

Table 6. Measured values for average FWHM of the capillary tube images for horizontal and vertical orientations.

	Capillary Tube Orientation and Location	Ave. Width of Cap. Tube Image (mm,FWHM)	Ave. System Extrinsic Spatial Resolution (mm FWHM)
LabRAT 0	horizontal, over mod. 2	4.88 +/- 0.4	
	horizontal, over mod. 3	4.97 +/- 0.5	
	vertical, over mod. 2	5.45 +/- 0.4	
	vertical, over mod. 3	4.56 +/- 0.6	4.96 +/- 0.6
LabRAT 1	horizontal, over mod.1	2.97 +/- 0.9	
	horizontal, over mod. 2	4.44 +/- 1.1	
	horizontal, over mod. 3	5.09 +/- 0.9	
	vertical, over mod 1/2	5.3 +/- 1.2	
	vertical over mod 2/3	5.15 +/- 0.8	4.59 +/- 1.1

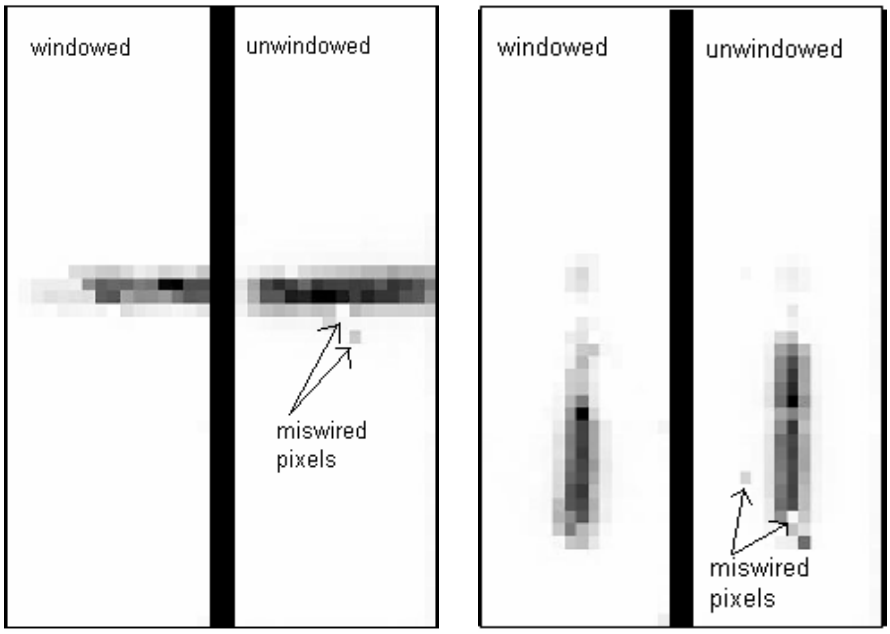

Figure 47. Windowed and unwindowed capillary tube images from LabRAT 1. Horizontal over module 2 is the orientation of the capillary tube relative to the detector for the two figures on the left, vertical over modules 2 and 3 is the orientation for the two on the right.

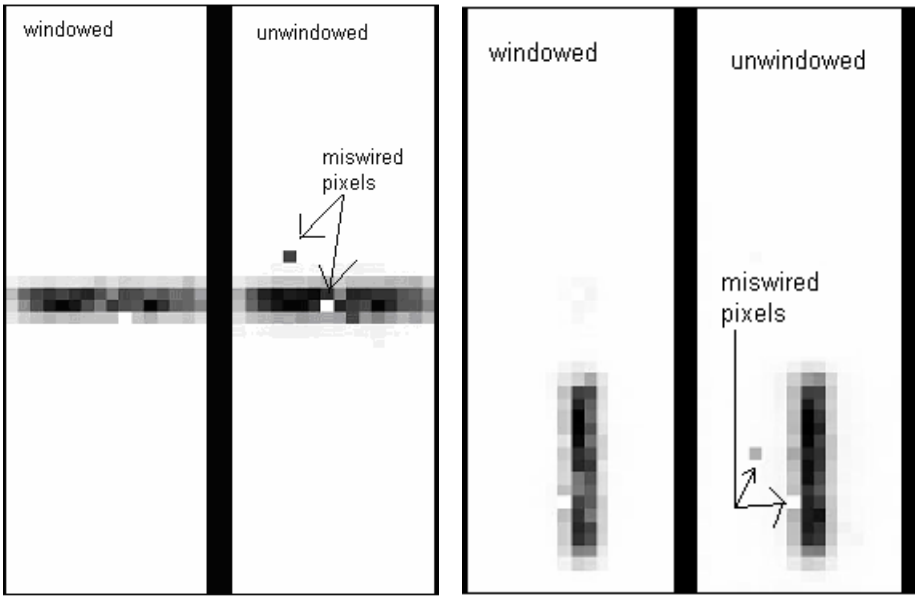

Figure 48. Windowed and unwindowed capillary tube images from LabRAT 0. Horizontal over module 2 is the orientation of the capillary tube relative to the detector for the two figures on the left, vertical over module 3 is the orientation for the two on the right.

5.4 Linearity

For these tests we used the same setup as the count rate measurements (section 5.1) but we placed a lead slit phantom against the detector face. Shown in Figure 49, the slit phantom is a 15 cm x 15 cm x 3.1 mm sheet of lead glued between 3.1 mm thick sheets of acrylic. Slits of 1 mm width spaced at 15 mm intervals are cut into the lead. The source was 2.3 mCi of Tc-99m placed at 100 cm distance from the detector. One million counts were acquired at each orientation (horizontally, vertically, diagonally) of the slit phantom.

Figure 49. Slit phantom for linearity measurements.

For the linearity measurements it is expected that if the slits are aligned to the rows or columns of pixels and a slit is located above a row or column of pixels, the windowed image will be contained within that single row or column of pixels. It is also expected that if the source lines up along the border between two rows or columns of pixels, the events will share signals between the rows or columns; many of these events

will have energies that fall in the tails of the photopeak so that after energy windowing is applied, many of the counts in these rows or columns will be rejected from the image. Also, there is a 1.2 mm (or half-pixel wide) gap between modules. We expected that the image of a diagonal orientation of the slit phantom might show a discontinuity in the image where two modules meet, because our image does not account for the physical gap. However, the pixelation of the detector overwhelms any chance of seeing this discontinuity. Figure 50 shows an image of the diagonal orientation of the slit phantom from LabRAT 0.

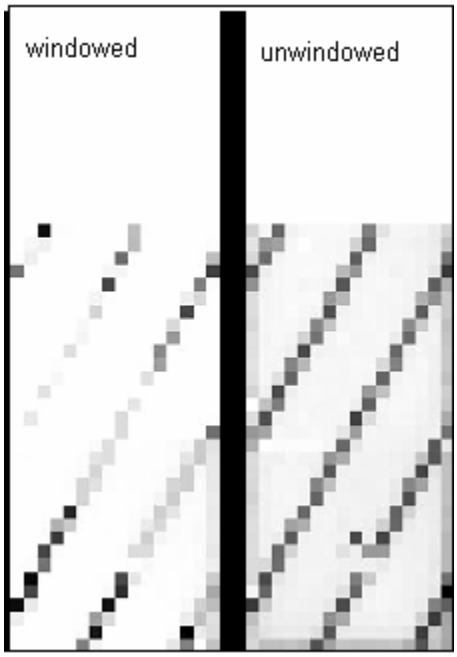

Figure 50. Windowed and unwindowed slit phantom images from LabRAT 0, showing a diagonal orientation of the phantom relative to the detector.

Table 7 shows the average fitted center locations for the vertical and horizontal orientations for both detectors. The center locations were obtained by fitting a Gaussian function to profiles perpendicular to the slits. The fitted centers for all profiles of a slit were then averaged. Figures 51 and 52 show the images for each slit orientation for the

two LabRAT systems, with the unwindowed data on the right and the images with the energy window applied on the left.

Table 7. Average fitted location of the slits in pixel coordinates for linearity tests using slit phantom in vertical and horizontal orientations for both the LabRAT systems.

		Ave. Fitted Center of the Slit (Pixel Coordinate)
LabRAT 1	Columns	36 +/- 0.1
		42 +/- 0.2
	Rows	33 +/- 0.1
		39 +/- 0.1
		45 +/- 0.1
		51 +/- 0.1
		57 +/- 0.1
LabRAT 0	Columns	36 +/- 0.1
		42 +/- 0.03
	Rows	36 +/- 0.01
		41 +/- 0.01
		48 +/- 0.02
		55 +/- .08
		61 +/- 0.01

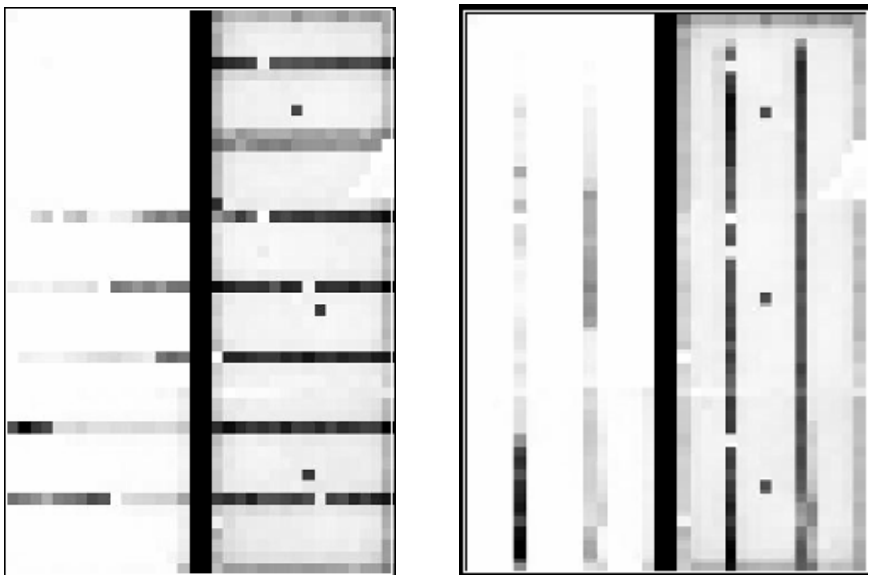

Figure 51. Slit phantom images from LabRAT 1. Horizontal orientation of phantom to the detector are the two images on the left, vertical orientation on the right. Windowed images are on the left of each pair, unwindowed on the right of each pair.

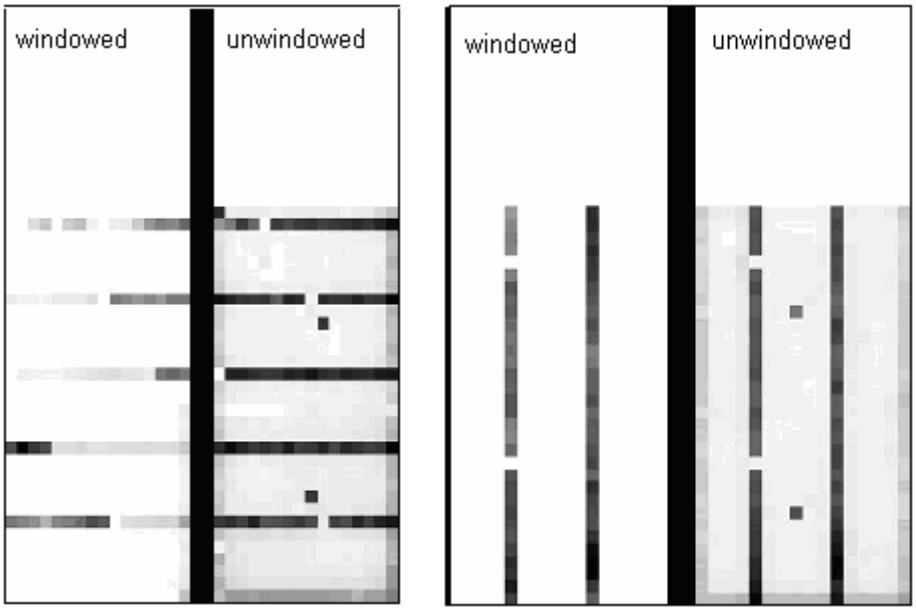

Figure 52. Slit phantom images from LabRAT 0. Orientation and windowing are the same as in Figure 51.

5.5 Integral and Differential Uniformity

Integral uniformity is defined as the difference between the maximum and minimum pixel values over the FOV for the entire detector. NEMA specifies differential uniformity as the largest difference between two pixels within any set of three contiguous pixels in a row or column of the flood-field image [3]. Uniformity is calculated as

$$Uniformity = \pm 100\% \frac{(\max - \min)}{(\max + \min)} \tag{6}$$

The maximum and minimum for this calculation are determined globally for integral uniformity and from every set of three contiguous pixels for differential uniformity. Thus, integral uniformity assesses the overall variation of the detector system while differential uniformity measures point-to-point variations.

For the uniformity measurements we filled a 15 cm x 15 cm x 1 cm volume acrylic water tank phantom (see Figure 53) with 2.8 mCi of Tc-99m. We placed the collimator piece over the modules on the face of the detector, surrounded the collimator with lead shielding and placed the water phantom over the collimator. This collimator setup is identical to that used for the extrinsic spatial resolution measurements; the detector setup is shown in Figure 54. The raw image from LabRAT 0 is shown in Figure 55.

The image data is smoothed with a nine point filter function as recommended by NEMA, after dead pixels had been replaced with the averages of their neighbors. NEMA also specifies a 15% energy window on the flood-field uniformity image data. When we applied the 15% per-pixel energy window to our data, the resulting images became exceptionally non-uniform. Presumably, the large distributed tank source results in many events at the edges of pixels; when this is the case the events fall in the energy spectra tails and are excluded after the energy windowing. (This effect likely occurs with any distributed source, even patients, and is an issue that must be dealt with for CZT gamma cameras.) Because of this we decided to use the unwindowed data for the uniformity measurements. Integral and differential uniformity were calculated for all pixels in the detector for both systems. For comparison, we also calculated the integral and differential uniformity for a field of view that excluded a 1-pixel wide margin at the detector edge with the justification, as previously mentioned, that pixels on the detector edges may exhibit abnormal response with respect to the rest of the detector. For LabRAT 1 we also eliminated three rows from the top and bottom of the image because the length of the collimator was shorter than the length of the three modules. These top

and bottom rows exhibited either no response (fully shielded by lead sheet) or extremely high response due to penetration between the collimator edge and the lead sheet. For the LabRAT 1 water tank data we calculated the uniformity values for the remaining rows of pixels as the full FOV and then removed the perimeter from these remaining rows to get the smaller FOV.

For the sake of comparison, the integral and differential uniformity was calculated for flood field data obtained using a Tc-99m point-source for both systems that had been acquired as part of the detector calibration data. The values calculated from the point source data indicate intrinsic uniformity (no collimator, point source at a distance > 5 times the FOV), while the values obtained from the water tank data indicate the extrinsic uniformity (using a collimator and a planar source). Table 8 summarizes the integral and differential uniformity results for both systems for the water tank and for the point-source flood field.

Figure 53. Water tank phantom used for system uniformity measurements.

Figure 54. Photograph of setup for extrinsic uniformity test including parallel hole collimator in the center, lead shielding around the collimator and the water tank phantom.

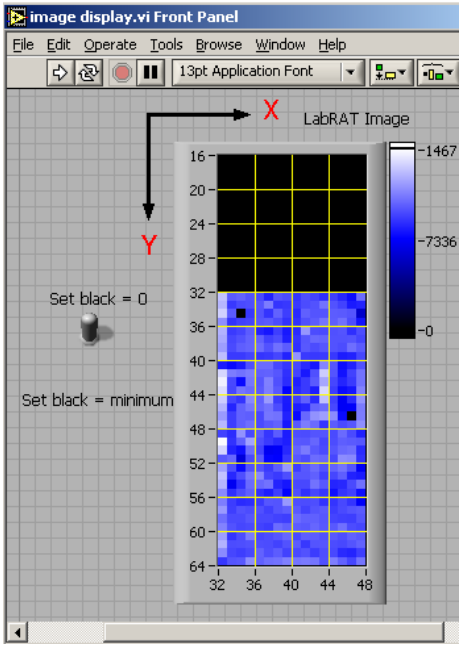

Figure 55. Unwindowed extrinsic flood image from LabRAT 0, 20 million counts.

Table 8. Integral and differential extrinsic uniformity values for the LabRAT systems for the entire detector FOV and for a smaller FOV that excludes a 1-pixel wide perimeter of edge pixels. The intrinsic uniformities, measured from a Tc-99m point source flood image used for detector tuning (Chapter 4), are shown for comparison.

		Integral Uniformity (%)	**Differential Uniformtiy (%)**
LabRAT 0 Water Tank Flood	Entire Detector	26.1	14.2
	Without Edge Pixels	19.2	15
LabRAT 1 Water Tank Flood	Entire Detector	38.6	21.1
	Without Edge Pixels	23.6	15.7
LabRAT 0 Intrinsic Point-Source Flood	Entire Detector	19.21	13.88
	Without Edge Pixels	16.73	11.52
LabRAT 1 Intrinsic Point-Source Flood	Entire Detector	28.3	19.4
	Without Edge Pixels	25.9	19.3

Chapter 6

Discussion and Conclusions

This chapter summarizes the performance characterization results for the LabRAT systems. Section 6.1 discusses the issue of dead and miswired pixels in the detector modules. In section 6.2 the results of the performance tests are discussed. Future work on the LabRAT systems and general comments on the utility of CZT gamma cameras are discussed in section 6.3.

6.1 Miswired Pixels

We discovered in the course of our research that the same four pixels were consistently bad in each module. Figures 56 and 57 show an entire module's worth of pixel spectra for each system to demonstrate the location of these four pixels. These abnormal pixels were not detected during the analysis of overall detector data such as the flood field or count rate studies where large groups of pixels were measured at once; the pixels seemed to function normally. It was not until we began to compare individual pixel spectra that we discovered this pattern. These pixels are connected consecutively to the 42^{nd} and 43^{rd} input circuits in each ASIC [7]. Their hexadecimal pixel values according to the pixel map (Figure 7) are 2A and 2B in ASIC 0 and AA and AB in ASIC 1. With 128 pixels connected to each ASIC, AA and 2A correspond to the same pixel in sequence but on opposite ASICs, as do AB and 2B. It appears that the pairs of pixels are miswired, presumably by swapping the bonding order when the module was manufactured. A collimated source placed under pixel AA shows up in the image display

for pixel AB and vice versa; pixels 2A and 2B are similarly swapped. All four pixels appear to function in a reasonably normal way, aside from misplacing events in their partner pixels. Fortunately, the fix for this is straight forward. In the acquisition software, any events measured in one of the pixels are specifically reassigned to the other pixel. (In point of fact, the fix is actually just a matter of altering the numbering scheme of the pixel map. The original error could even have been typographical in the documentation rather than a manufacturing issue.) In any case, the issue is common to all of these modules and is particularly troublesome because it does not show up on routine flood images but could cause misinterpretation of patient images.

We discovered this late in the data analysis. Therefore, all of our data was acquired with this problem. For the extrinsic spatial resolution, integral and differential uniformity and linearity images we manually swapped the pairs of pixels in each image before performing the analysis. The pixel map has now been altered to exchange the pixel pairs, so future acquisitions will not have this problem. There are other noisy and dead pixels in each detector, sometimes needing to be disabled, but aside from these four pixels the others seem to be random failures.

6.2 Discussion of NEMA Performance Test Results

6.2.1 Count Rate

The count rate studies were not fully accomplished due to the saturation of the detectors at such a low count rate. As was discussed in section 5.1, we were able to determine from the trigger signal that much higher count rates can be measured and it is yet to be determined the exact source of the count rate limitation, whether it is a problem with the National Instruments acquisition cards or the LabRAT software. It appears that

at low activities (below the 3000-3500 cps saturation level) both detectors exhibit normal behavior (see Figures 29 and 30) and it is expected that if the count rate limitation is removed, the 20% count loss and maximum count rate would be readily obtainable.

6.2.2 Energy Resolution and Uniformity of Detector Response

One of the primary incentives to use CZT as a detector material is the lure of better energy resolution than one gets from NaI(Tl). The crux of the problem with this type of pixellated detector module is that the average per-pixel energy resolutions for our detectors were 7.0% (LabRAT 0) and 6.48% (LabRAT 1), but the composite energy resolutions for the detectors were 27% and 40% respectively even after tuning. Admittedly, there may be some room for improvement within our tuning technique, but with the ASIC design used for the CZT modules in this system, the amount of control the user has over fine tuning is limited to gross ASIC-wide and module-wide adjustments.

A consistent pattern was noticed when comparing the data obtained from LabRAT 1 with that from LabRAT 0. Overall, the older-version ASICs used in LabRAT 0 are decidedly more consistent in their per-pixel energy spectra (see section 5.2.1). The new version ASICs in LabRAT 1 are also uniform in their spatial response, but vary widely in the photopeak center locations. The older version ASICs of LabRAT 0 have slightly poorer per-pixel energy resolution, but are more consistent in the location of the photopeak center from pixel to pixel. The better composite energy resolution for LabRAT 0 is a direct result of this. Probable sources of variation for photopeak channel number and detector response are the ASIC electronics and defects in the crystal that affect charge collection efficiency.

The difference between the two detectors must be a result of the change in ASIC design; LabRAT 0 uses 3.0 version ASICs and LabRAT 1 uses 3.2 version ASICs. It is expected that near the boundaries between two pixels, charge sharing will reduce the counts in both of the pixels; near the center of a pixel most of the counts will contribute to that pixel. This expectation was confirmed in our research as demonstrated in Figures 42 and 43.

6.2.3 Extrinsic Resolution

A collimator is a necessary part of being able to accurately reconstruct position information in images obtained in nuclear medicine. Ideally and necessarily, a given detector system will be equipped with a collimator that conforms to the specifications of that system. The LabRAT systems currently do not have collimators designed specially for them, this is part of the future work to be done on this system. What was used as a collimator in these extrinsic resolution measurements was a piece of low-energy all-purpose parallel hole collimator. One source of error in this may include the fact that the collimator that we used had hexagonal holes and the LabRAT detector pixels are square. Another source of error comes from the fact that ideally the holes in the collimator would be aligned as precisely as possible to the pixels to prevent Moire patterns through interaction of the pixel and collimator lattices [27]. Ideally, the lead septa in the collimator would cover the boundaries between pixels, but such precision alignment was not possible for our study using an unmatched collimator.

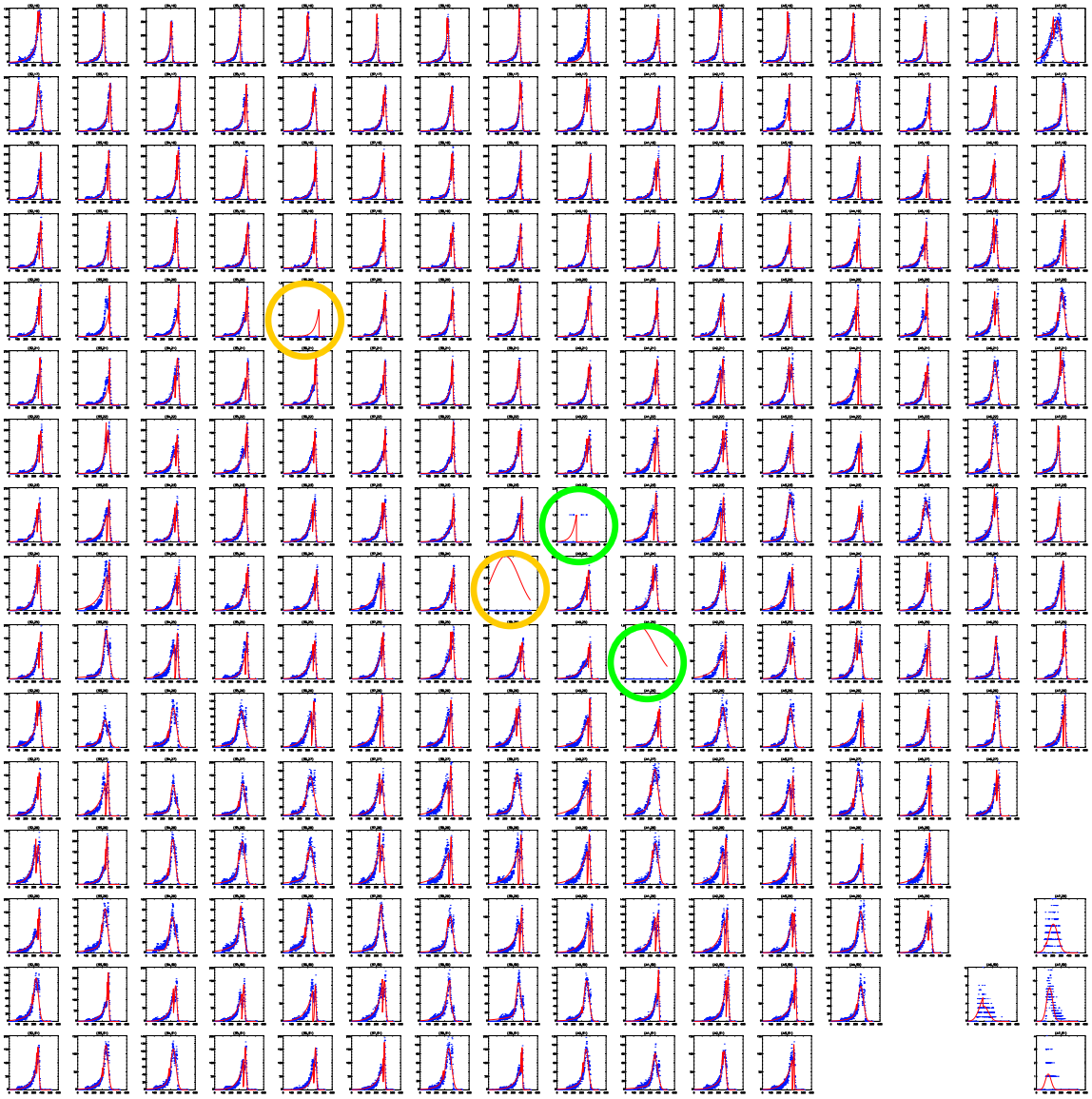

Figure 56. Per-pixel energy spectra (blue) and fitted spectra (red) for module 1 of LabRAT 1. The four miswired pixels are circled in the figure with the 2A/2B pair circled in orange and the AA/AB pair circled in green. In the lower right hand corner is a group of pixels that were disabled due to noisy behavior.

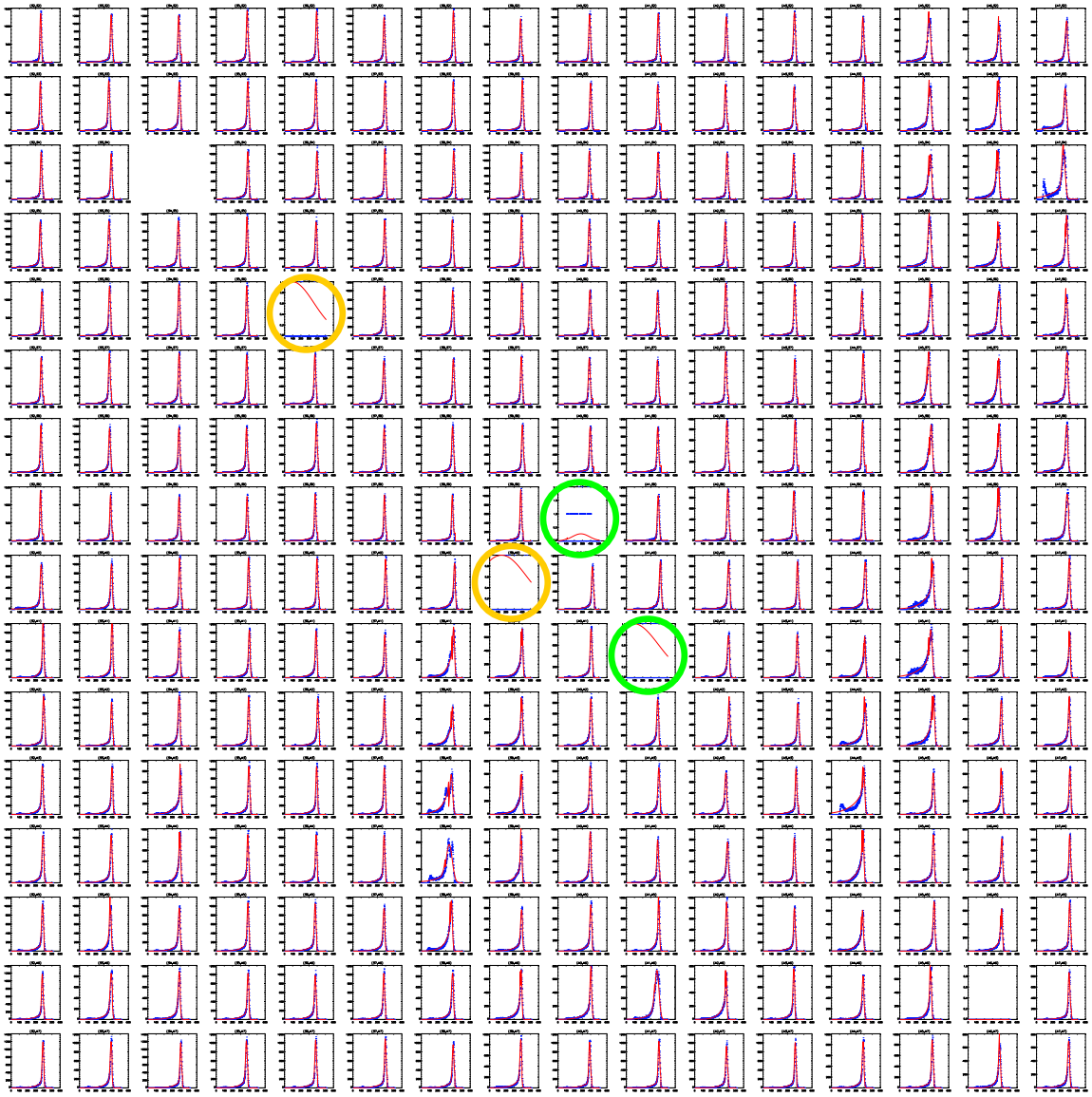

Figure 57. Per-pixel energy spectra (blue) and fitted spectra (red) for module 3 of LabRAT 0. The four miswired pixels are circled in the figure with the 2A/2B pair circled in orange and the AA/AB pair circled in green.

The intrinsic resolution for these detectors is limited to the pixel size of 2.4 mm. The extrinsic resolution is a measurement of the intrinsic resolution for a detector combined with the collimator resolution. The two resolutions add in quadrature. An approximate value for the geometric resolution of the collimator was calculated from [28]

$$Geometric\,collimator\,resolution = \frac{D}{T}\left(T + B + F\right) \qquad (7)$$

where $D = hole\,separation = 1.5\,mm$,

$T = collimator\,height = 23\,mm$,

$B = collimator - detector\,separation = 2\,mm$, and

$F = source - collimator\,distance = 50\,mm$.

The approximate geometric resolution for our piece of collimator with the given parameters is 4.9 mm. The expected FWHM extrinsic resolution value is therefore approximately 5.4 mm, compared to our measured value of 5.0 mm FWHM for LabRAT 0 and 4.6 mm FWHM for LabRAT 1. The extrinsic resolution was reasonably consistent and within expectations for the various orientations and across the different modules within each detector.

6.2.4 Linearity

The fact that the CZT modules used in the LabRAT systems are arranged into 16 x 16 arrays of pixels forces linearity onto the system that would not be present in a NaI(Tl) detector system. If radiation interaction events occuring within an individual pixel were guaranteed to be collected in that pixel, measuring linearity for CZT would be redundant. However, charge sharing near the boundaries between pixels creates a distribution of counts about that single pixel. The individual standard deviations of the linearity measurements tended to be a bit larger for LabRAT 1 than LabRAT 0, but the

variation among the standard deviations was much worse for LabRAT 0 than LabRAT 1. This is another demonstration that the older ASIC design in use in LabRAT 0 exhibits better energy resolution but slightly worse uniformity in spatial response than the newer ASICs of LabRAT 1.

6.2.5 Integral and Differential Uniformity

Given that the uniformity of response for LabRAT 0 seems slightly worse, it would seem that the integral uniformity should be worse for LabRAT 0 than for LabRAT 1. This was not the case; in fact the integral and differential uniformity for the water tank flood field was better for LabRAT 0 than either the water tank flood field or the point source flood field uniformities for LabRAT 1. The differential uniformities were less than the integral uniformities in all cases as is expected because differential uniformity measures count magnitude variations on the small scale (over 3 contiguous pixels) while integral uniformity measures the maximum-minimum variation over the entire detector. Removing the data for the outer perimeter of pixels consistently improved the integral uniformity, but had less of an effect on the differential uniformity. It has been reported that the edge pixels may generally respond differently than the rest of the detector, so the improvement in integral uniformity by removing them is consistent with that observation.

6.3 Future Work

CZT is a promising radiation detector material and LabRAT has potential to be a valuable nuclear medicine imaging device. There are some adjustments that could be made to further improve the LabRAT systems, as well as other tasks to be addressed that were not included in this study.

1. Improve tuning: whether it is possible for the manufacturer to improve the detector module ASICs to enable more precise fine tuning is not known to us, but such improvement would be highly desirable. There is still some room for improving our current tuning routine discussed in Chapter 4.
2. Do linear interpolation for noisy pixels with low counts, or diabled pixels: For some of our results, we inserted (post-acquisition) average values into noisy or dead pixels from neighboring pixels. This could be automated for detector-wide implementation during acquisition and perhaps with more sophistication than simply using average values.
3. Normalize images to the flood field by dividing acquired images by a high-count flood field. This will improve visually the spatial uniformity, although it is less desirable than improving the inherent uniformity.
4. Solve the problem of the low count rate saturation levels.
5. Experiment with asymmetric energy windows: Due to the tailing on the low energy side of the photopeak which creates asymmetric energy spectra, it seems more appropriate to accommodate this asymmetry during energy windowing. Asymmetric windows are used on NaI(Tl) gamma cameras occasionally, but not routinely.
6. Design a collimator suited for use with LabRAT.

CZT continues to be a promising detector material. Pixellation presents some difficulties with regard to tuning and the overall visual quality of images. Smaller pixels would make the images more visually appealing. The current ASIC design in the

LabRAT systems would be improved by having greater control over tuning of individual pixels. The LabRAT systems had reasonable spatial resolution and per-pixel energy resolution, but overall energy resolution and uniformity were somewhat disappointing. In all, continued improvements of CZT detector systems are probably warranted and CZT gamma cameras will likely become a useful alternative to NaI(Tl) cameras for small FOV applications.

References

1. Matthews, K.L.II., Development and Application of a Small Gamma Camera. PhD.Thesis, The University of Chicago, 1997.

2. Shah, K.S., Glodo,J., Klugerman,M., Higgins,W., Gupta,T. and Wong,P. High Resolution Scintillation Spectrometers. Retrieved Feb 2005 from http://www.rmdinc.com/papers/HighEnergyResolutionScint.pdf

3. NEMA NU 1 Performance Measurements for Scintillation Cameras. 2001. Rosslyn,Va.

4. Schlesinger, T.E. and James, R.B. (eds). **Semiconductors for Room Temperature Nuclear Detector Applications.** Vol. 43. Academic Press, San Diego, 219-378, 1995.

5. Knoll, Glenn F. **Radiation Detection and Measurement 3rd edition.** John Wiley & Sons Inc., New York, 2000.

6. Wagenaar, D.J. CdTe and CdZnTe Semiconductor Detectors for Nuclear Medicine Imaging. In: **Emission Tomography, The Fundamentals of PET and SPECT.** Wernick, M.N. and Aarsvold, J.N. (eds). Elsevier Academic Press, San Diego, 269-291, 2004.

7. Sobotka, L., Cadmium Zinc Telluride (CZT) Detectors. Power Point Presentation. http://www.pas.rochester.edu/~cline/ria/Reviol.pdf#search='spatial%20resolution%20imarad%20CZT'

8. Perkins, J., Krawczynski,H., Dowkontt,P. and Leopold,D.Development of Low Cost Thick CZT Detectors. Power Point Presentation. Retrieved Dec. 2004 from http://jelley.wustl.edu/~jperkins/cztposter.pdf

9. Butler, J.F., Friesenhahn, S.J., Doty, F.P., Ashburn,W.L. Conwell, R.L., Augustine, F.L., Apotovsky, B., Pi,B., Collins,T., Zhao, S., and Isaacson, C. CdZnTe Solid State Gamma Camera. **IEEE Trans Nucl. Sci., 45**:2, 359-363, 1998.

10. --. **XAIM 3.2 Documentation v0.91. 2001. p. product manual.** Integrated Detector and Electronics AS, Ideas. Fornebu,Norway. www.ideas.no, Retrieved March 2005 from http://www.ideas.no/products/DAQs/pdf/XA-Controller-ReadOut-System-Instructions-V1R6.pdf

11. Sato, G., Parsons, A., Hullinger, D., Suzuki, M., Takahashi, T., Tashiro, M., Nakazawa, K., Okada, Y., Takahashi, H., Watanadbe, S., Barthelmy, S., Cummings, J., Gehrels, N., Krimm, H., Markwardt, C., Tueller, J., Fenimore, E., Palmer, D. Development of a Spectral Model Based on Charge Transport for the Swift/Bat 32K CdZnTe Detector Array.. Preprint submitted to Elsevier Science, 2004. Retrieved Feb. 2005 from http://www.astro.isas.ac.jp/~takahasi/DownLoad/NIM2004-Sato-STD-Paper.pdf

12. Kalinosky, M.A., Wagenaar, D.J., Burckhardt, D., and Engdahl, J.C. Pixel-pixel interactions in a square pixel array CdZnTe detector. **Med. Phys. 27** (6) :1380, 2000.

13. Slavis, K., Dowkontt,P., Duttweiler, F., Epstein, J., Hink,P., Huszar, G., Leblanc, P., Matteson, J., Skelton,R., and Stephan, E. Background Studies of a Position Sensitive CdZnTe X-ray Detector at Balloon Altitudes. **SPIE Proc. 3445**, 169, 1998. Retrieved Feb.2005 from http://cosray2.wustl.edu/HEXIS/ICRC99/OG4_1_14.pdf#search='matteson%20CZT'

14. Altice, P.P., Cherry, M.L., Band, D.L., Buckley,J., Guzik,T.G., Hink,P.L., Kappadath,S.C., Macri,J.R., Matteson,J.L., McConnell,M.L., Ryan,J.M., Slavis,K.R. and Stacy, J.G. MARGIE-Minute of Arc Resolution Hard X-Ray/Gamma Ray Imaging Telescope For an Ultra Long Duration Balloon Mission. **Advanced Space Research,30**(5) 1321-1332, 2002.

15. --. **CZT Module Product Manual.** Imarad Imaging Systems Inc.Rehovot,Israel. www.imarad.com

16. --. Personal radiation detectors. **eV Products Homeland Security Applications Product Descriptions**. eV Products. Retrieved June 2005 from http://www.evproducts.com/pers_rad_detec.html

17. --.Palm sized radiation detector, the Los Alamos CZT spectrometer. **Los Alamos National Lab News and Public Affairs.** Los Alamos National Lab. Retrieved Oct. 2004 from www.lanl.gov
18. --. Rad-ID Advanced Technologies for Homeland Security. **Dtect systems Product Specifications.** Dtect Systems. Retrieved Oct. 2004 from http://www.dtectsystems.com/dtectdocs/rad-ID%20specs.pdf

19. Narita, T. Grindlay, J.E., Jenkins, J.A., Perrin, M., Marrone, D., Murray, R. and Connell, B. Design and Preliminary Tests of a Prototype CZT Imaging Array. Harvard-Smithsonian Center for Astrophysics. **Proc SPIE, 4497**:79, 2002.

20. Mueller, B., O'Connor, Michael K., Blevis, Ira, Rhodes, Deborah, Smith, Robin, Collins, Douglas A. and Phillips, Stephen W. Evaluation of a Small Cadmium Zinc Telluride Detector for Scintimammography. **Journal of Nuclear Medicine 44**(4): p. 602-609, 2003.

21. Vidal-Sitjes, G., Baldelli, P. and Gumbaccini, M. A CdZnTe Pixel Detector for Bone Densitometry. **Nucl. Inst. Methods in Phys. Res. A 518,** 401-403, 2004.

22. Scheiber, C. and Giakos, G.C. Medical Applications of CdTe and CdZnTe Detectors. **Nucl. Inst. Methods in Phys. Res. A 458**, 12-25, 2001.

23. --.National Instruments LabView. National Instruments Corp. Austin,TX. www.ni.com

24. --. IDL Research Systems Inc. Boulder,Co. www.rsinc.com/idl/

25. --. **Users Guide NF90 Series.** Velmex, Inc.Bloomfield,NY. www.velmex.com

26. Keyser, R.M. Characterization of Room Temperature Detectors using the proposed IEEE Standard. **IEEE Nucl. Sci. Symp. Med. Imag. Conf. Rec.** 2001.

27. Gunter, D.L, Matthews II, K.L. and Ordonez, C.E. The Interaction of Collimator Lattice Periodicity and Detector Pixellation. **Conference Record of the 1998 IEEE NSS/MIC,** paper M07-54, 1998.

28. Gunter, D.L. Collimator Design for Nuclear Medicine. In: **Emission Tomography, The Fundamentals of PET and SPECT.** Wernick, M.N. and Aarsvold, J.N. (eds). Elsevier Academic Press, San Diego, 153-168, 2004.

Appendix A

Spatial Resolution Software

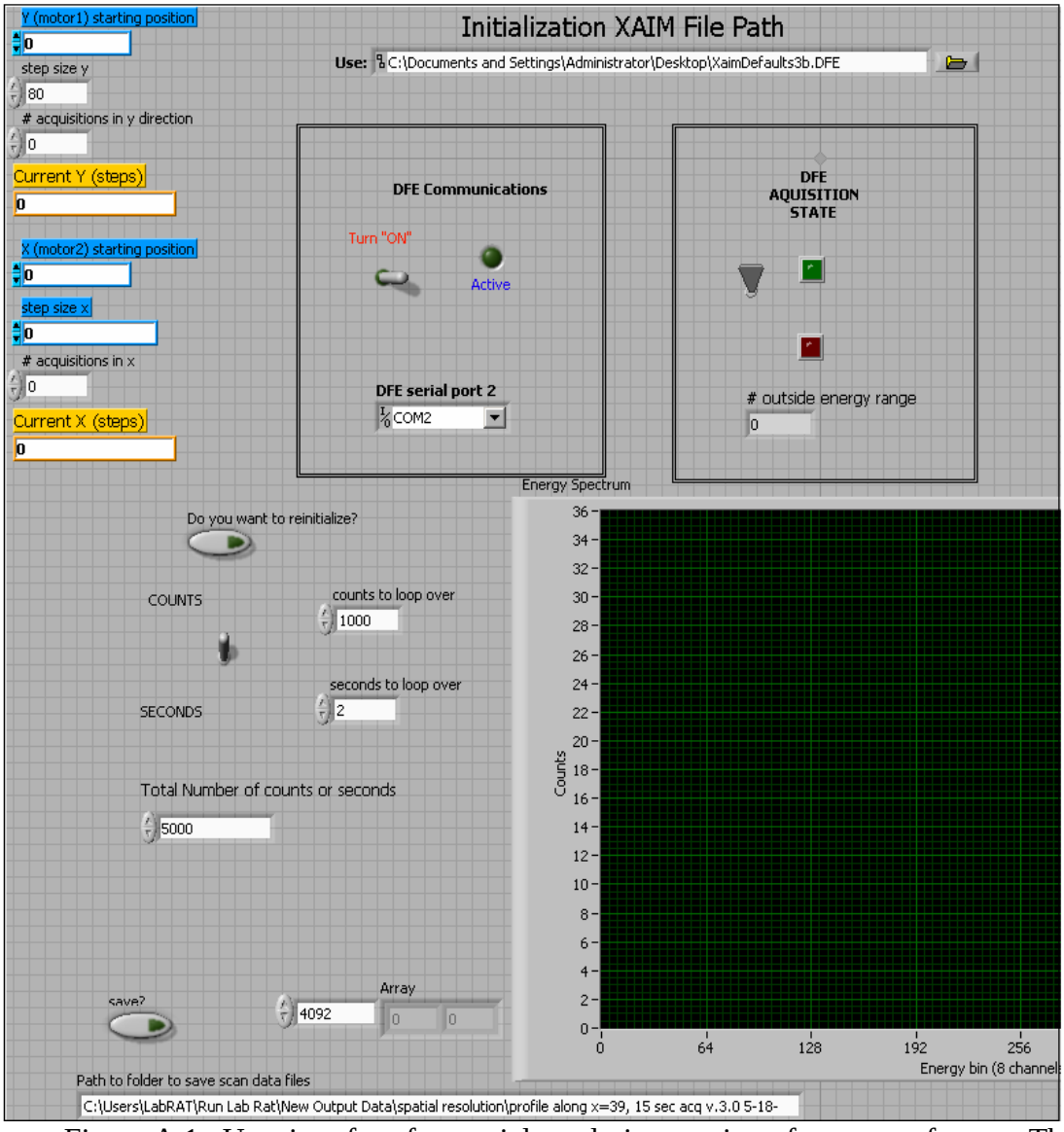

Figure A.1. User interface for spatial resolution version of system software. The main difference is the addition of controls to run the translation stage (seen in upper left).

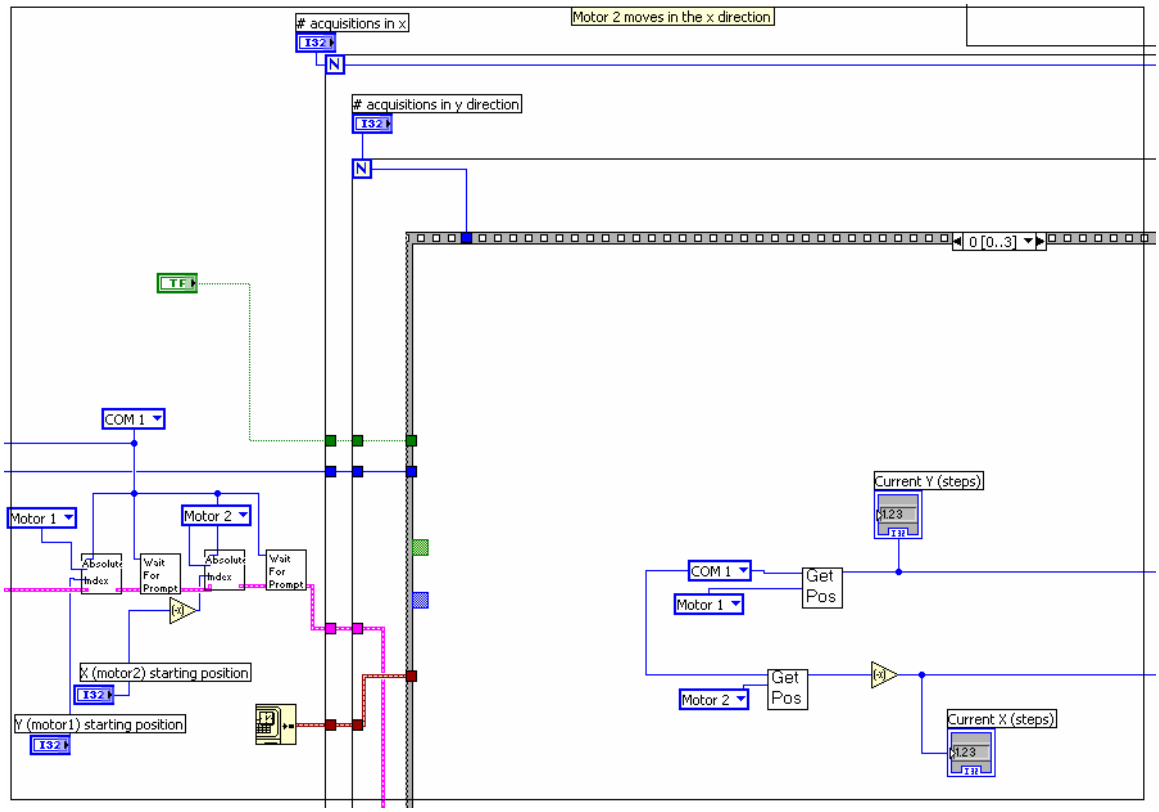

Figure A.2. Partial view of one loop of spatial resolution block diagram. Subprograms to initialize translation stage can be seen outside the loop to the left. The Get Pos boxes inside the loop get the current motor positions of the translation stage.

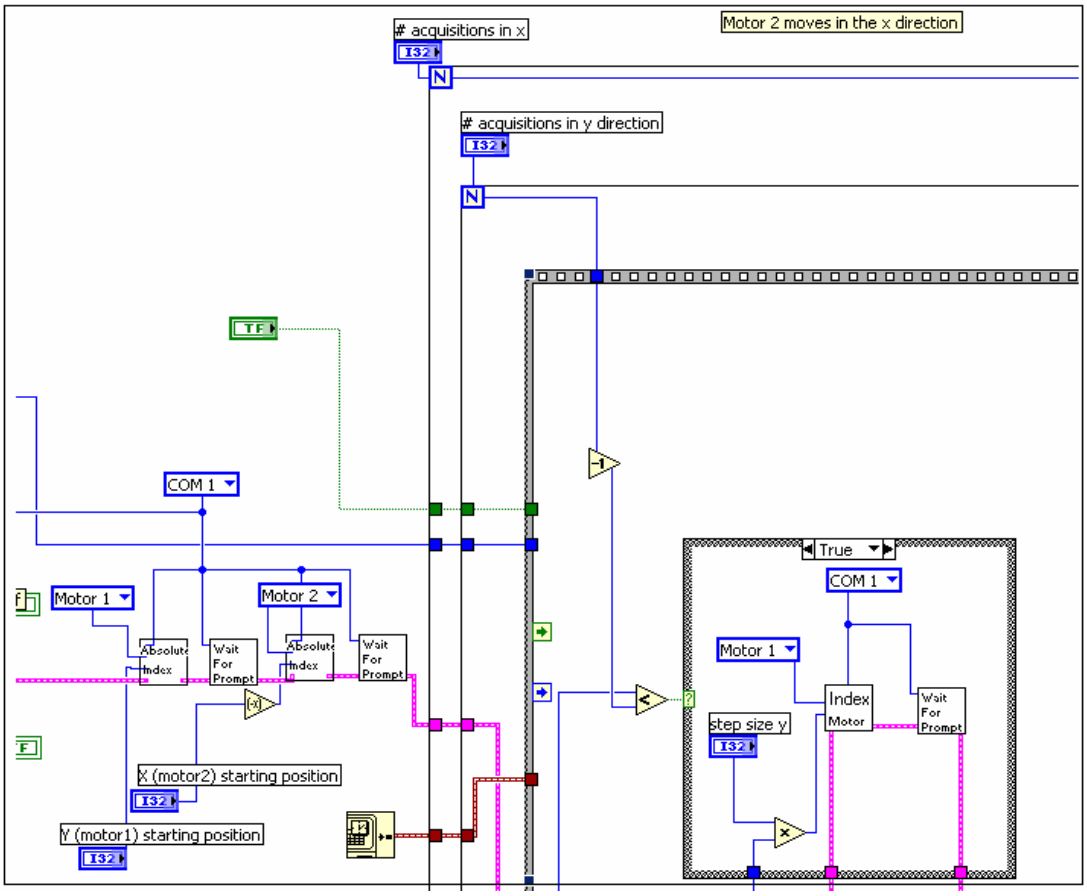

Figure A.3. Partial view of another loop of the spatial resolution block diagram. The Index Motor box within the loop takes values from user input controls and moves the translation stage motors to the desired positions.

Appendix B

LabRAT Block Diagrams

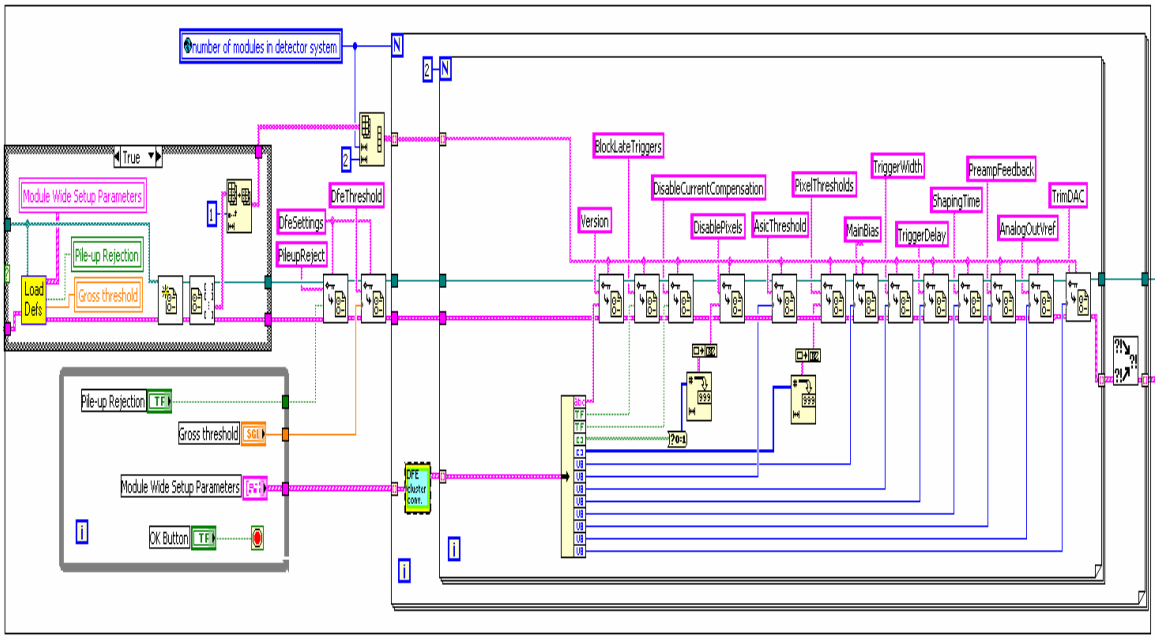

Figure B.1. MakeDFEDefaults block diagram.

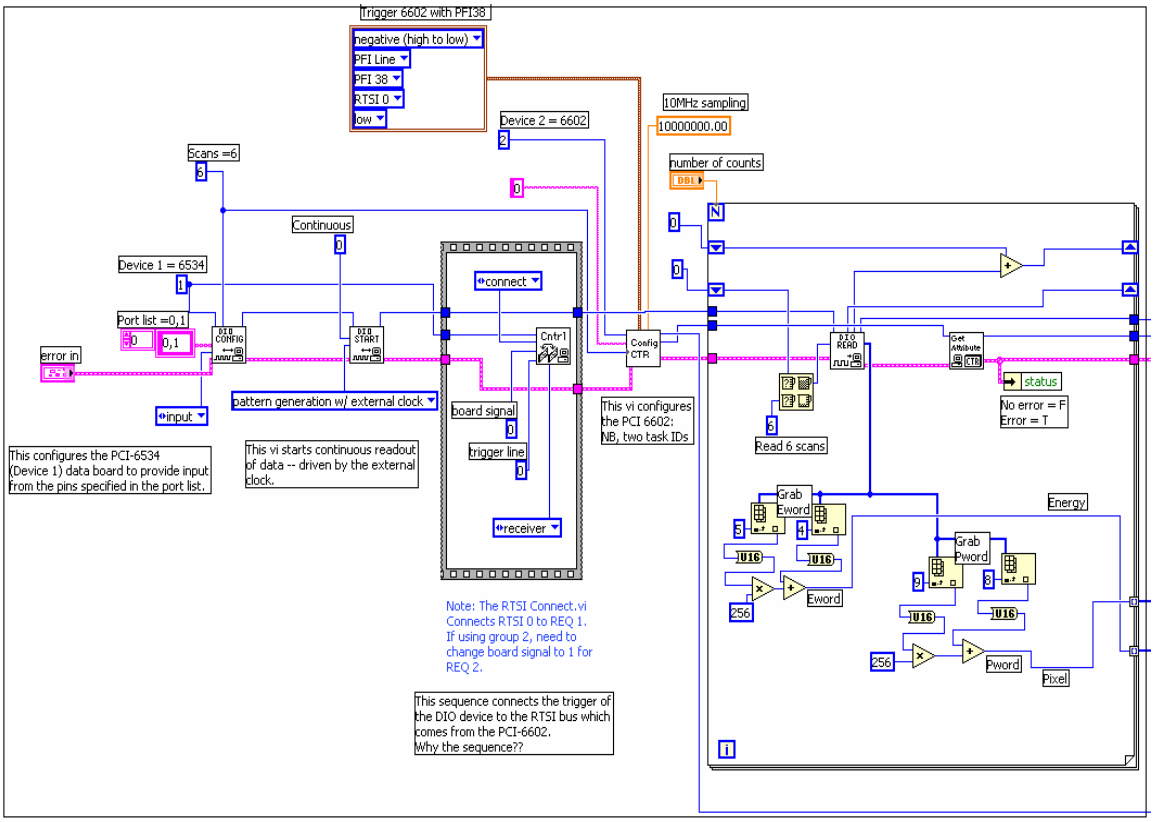

Figure B.2. Events2Disk block diagram.

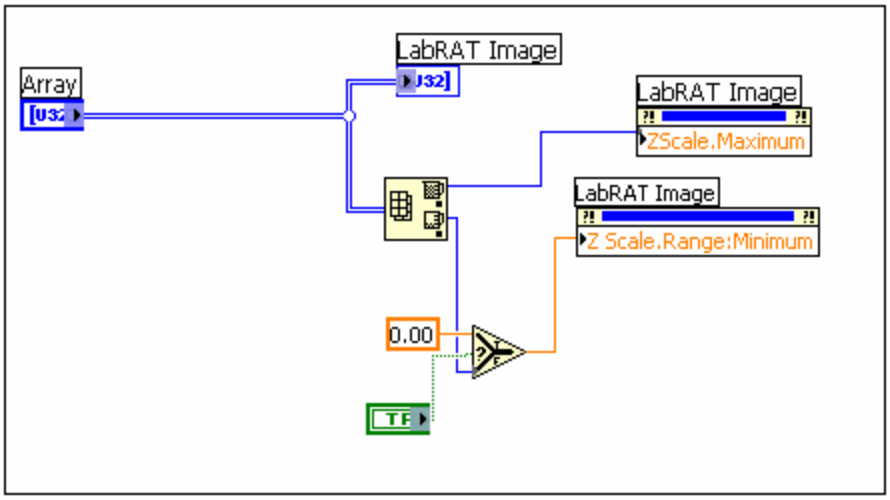

Figure B.3. Image display block diagram.

Appendix C

Detector Initialization Parameters

a) ASIC version: During the course of development, IMARAD the company which produces the CZT modules, had updated from a 3.0 version module to a 3.2 version module. In the prototype detector we have two 3.0 version modules. In the newer detector we have one 3.0 version module and three 3.2 version modules in our detector. The main difference between the versions is a Trim Dac control which allows the user to define the step size for other parameters. For instance the user can adjust the voltage threshholds for individual ASICS using a control called vthr. If TrimDac is set to zero, the input for vthr is multiplied by a factor of 1.5. If TrimDac is set to one, the input for vthr is multiplied by a factor of 1, and so on up to a multiplicative factor of 3. Although the newer detector contained one earlier 3.0 version module without the TrimDac capability and we programmed the software to accomodate both versions, the 3.0 version module did not work in this detector. We were unable to determine if there had been some damage to this module. By the time we ran the NEMA tests, we took the 3.0 version module out of the newer detector, so we had one detector with three 3.2 version modules and one detector with two working 3.0 version modules.

b) Disable current compensation: When I started working on this project all of our default input files used a value of true for this setting. We assumed this to be correct. We reached a point in programming where everything should have worked and we could not get the detector to run properly. Dr. Matthews went to Chicago and obtained the prototype version of the detector (3.0 version modules)

he had worked on there complete with the same initialization software and input files that we had started with. After an extensive analysis of the software for this earlier prototype, we realized that the one difference was that the disable current compensation parameters were all set to false instead of true in the input files. Once we undertook the simple task of changing this one parameter the detector was able to run successfully.

c) Pile up rejection: We always set this to true. It ignores subsequent radiation events until the detector has finished processing earlier events.

d) Pixel enable/disable and individual pixel threshholds: There are 256 pixels per CZT module. Each pixel has its own circuitry associated with detecting incoming radiation events. There is variation among the pixels in the amount of electronic noise present as well as inherent variations in pixels due to imperfections in the structure of the crystal resulting from the fabrication process. These variations lead to heterogeneity in the individual spectra produced by different pixels which leads to a broadening of the overall energy spectrum obtained for a given module and the detector as a whole. It is necessary to tune the pixels so that they are more homogenous in their response to the same signal in order that the energy resolution of the system as a whole not be degraded. Most pixels, even if they have a large variation from the average response can be tuned by adjusting a combination of the vthr (ASIC wide threshhold) , gross threshhold (detector wide threshhold) and individual pixel threshhold. However, some pixels have bad electrical connections either resulting from damage or improper fabrication. This can result in a noisy pixel due to arcing at the area of

the bad connection and results in this pixel having such a higher number of events than the rest of the module that all other pixels are washed out and the entire energy spectrum is dominated by this noise. In this case the pixel can be turned off. In addition, the individual pixel threshhold controls are simply not very effective. Perhaps the variation in energy is too fine for the detector to show much response.

For both the pixel enable/disable and the individual pixel threshholds the method for adjustment prior to the start of my work was to go into the input file and look for the binary number which corresponds to that pixel and manually change it. The problem with this method is that the input file is just a text file with the different parameters and for pixel enable/disable and individual pixel threshholds there is just a string of 128 ones and zeros for each ASIC. To change one pixel, you had to count across the line until you got to the pixel you were looking for. This method was error prone. We modified this by creating arrays of controls, one for pixel enable/disable and one for individual pixel thresh holds, containing an LED or a digital control for each pixel. The array of controls is set up in a sixteen by sixteen square replicating the arrangement of pixels in the module and labeled accordingly. The user must still manually find and adjust the control for a given pixel, but this arrangement is easier and more accurate. The user controls for pixel enable/disable and pixel thresholds can be seen in figure 2.4a.

e) DFE thresh hold: This parameter sets the gross voltage thresh hold for the entire detector.

f) ASIC thresh hold: This parameter is a finer voltage adjustment, sets thresh hold for individual ASICs. This is added or subtracted to the DFE thresh hold.

The other parameters in the input file are the ASIC number, main bias, trigger width, trigger delay, shaping time, preamp feedback, analog out voltage reference. These other parameters were tested and seemed to have little effect on the output of the detector, therefore they have a default setting of zero and are always set to zero.

Vita

Laurie Kelly was born in Pennsylvania but does not remember anything about Pennsylvania. She has lived in Farwell and Paw Paw Michigan, Truckee California, Reno Nevada, New Orleans and Baton Rouge Louisiana, and will soon move to Memphis Tennessee. After graduating from high school she enjoyed three interesting and happy years traveling across the United States, supporting herself by selling jewelry and other crafts. She became disillusioned with government altruism after a stint as an Americorps volunteer. Other jobs she has held are fast food cashier, waitress, factory worker, construction worker, office worker, video store clerk, casino buffet hostess and maid as well as student and research assistant and will soon be employed as a medical physicist. She received her bachelors in physics from the University of New Orleans in December of 2002 and started work on her master's in medical physics at Louisiana State University the following month. She is the proud mother of a lovely seven year old daughter, Sophia Surreal Davis, who has been with her throughout her entire higher education journey.